iScience

CellPress
OPEN ACCESS

Article

Renal neoplasms in tuberous sclerosis mice are neurocristopathies

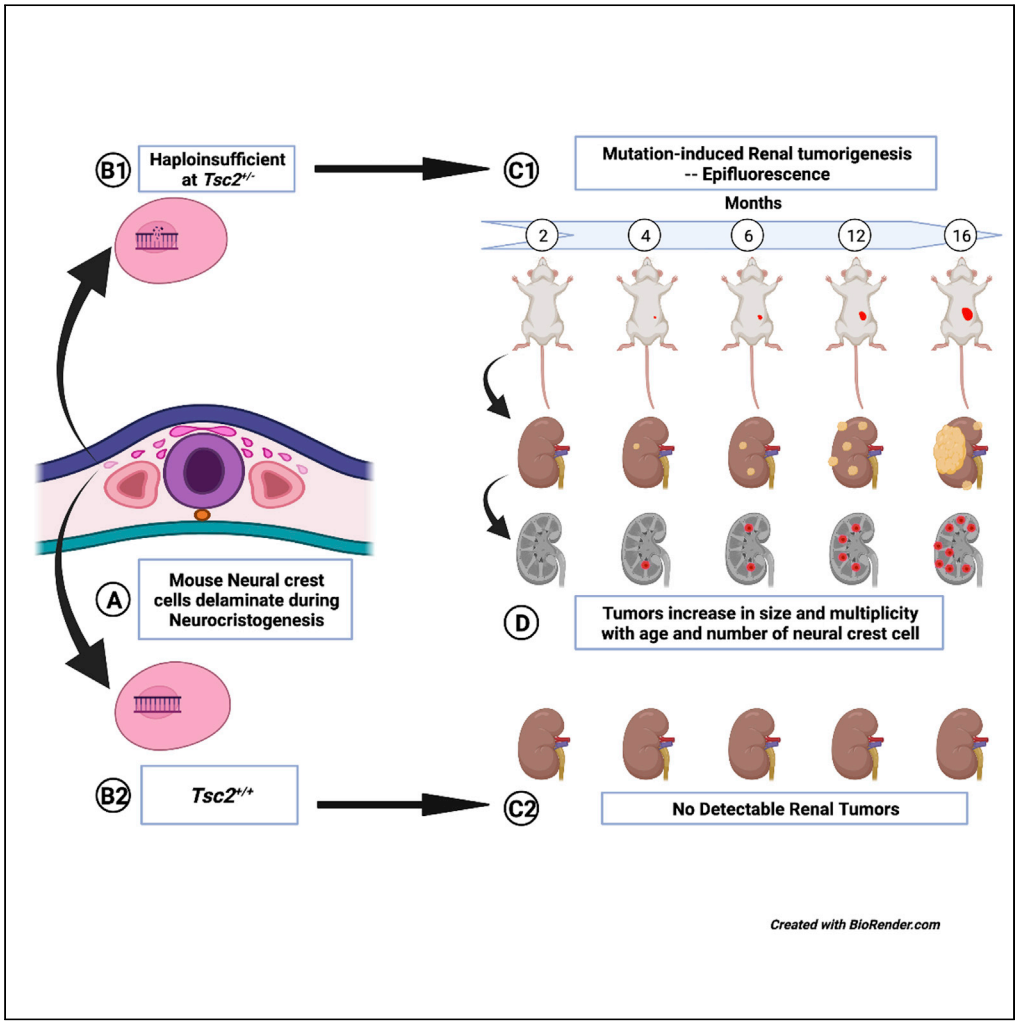

Uchenna Unachukwu, Takayuki Shiomi, Monica Goldklang, Kiran Chada, Jeanine D'Armiento

jmd12@cumc.columbia.edu

Highlights

Renal and hepatic tumors in $Tsc2^{+/-}$ mice comprise of neural crest cells (NCCs)

NCC proliferation increased with $Tsc2^{+/-}$ mice tumor volume and multiplicity

Multipotent $Tsc2^{+/-}$ NCCs induce tumors in ectodermally derived and non-neural tissues

Pharmacologically targeting NCCs offers an alternate treatment for tuberous sclerosis

Unachukwu et al., iScience 24, 102684
July 23, 2021
https://doi.org/10.1016/j.isci.2021.102684

iScience

CellPress
OPEN ACCESS

Article

Renal neoplasms in tuberous sclerosis mice are neurocristopathies

Uchenna Unachukwu,[1] Takayuki Shiomi,[2] Monica Goldklang,[1] Kiran Chada,[3] and Jeanine D'Armiento[1,4,*]

SUMMARY

Tuberous sclerosis (TS) is a rare disorder exhibiting multi-systemic benign neoplasms. We hypothesized the origin of TS neoplastic cells derived from the neural crest given the heterogeneous ecto-mesenchymal phenotype of the most common TS neoplasms. To test this hypothesis, we employed Cre-loxP lineage tracing of myelin protein zero (Mpz)-expressing neural crest cells (NCCs) in spontaneously developing renal tumors of *Tsc2*$^{+/-}$*/Mpz(Cre)*/TdT$^{fl/fl}$ reporter mice. In these mice, ectopic renal tumor onset was detected at 4 months of age increasing in volume by 16 months of age with concomitant increase in the subpopulation of tdTomato^{+} NCCs from 0% to 6.45% of the total number of renal tumor cells. Our results suggest that *Tsc2*$^{+/-}$ mouse renal tumors arise from domiciled proliferative progenitor cell populations of neural crest origin that co-opt tumorigenesis due to mutations in *Tsc2* loci. Targeting neural crest antigenic determinants will provide a potential alternative therapeutic approach for TS pathogenesis.

INTRODUCTION

Tuberous sclerosis (TS) is characterized by highly variable benign neoplasms and hamartomatous lesions in the brain, skin, heart, lungs, and kidneys (Dabora et al., 2001), seizures, and TS-associated neuropsychiatric disorders (de Vries et al., 2015). Heterozygous mutations of the tuberous sclerosis genes *TSC1* or more frequently *TSC2* have been causatively linked to the abnormal cytological proliferation characterizing tumors in patients with TS (Carsillo et al., 2000; Giannikou et al., 2016; Jones et al., 1999; Sato et al., 2002; Smolarek et al., 1998; Yu and Henske, 2010); however, not all tumors exhibit mutations in these genes (Sancak et al., 2005; Tyburczy et al., 2015). These *TSC1/2* mutations lead to hyperactivation of the mechanistic target of rapamycin (mTOR) pathway in a subset of the tumors (Clements et al., 2015; Goncharova et al., 2002), which have since informed the Food and Drug Administration-approved use of mTOR inhibitors for treatment of TS (Barrera et al., 2013; Bissler et al., 2008; Franz et al., 2013; McCormack et al., 2011). Although inhibition of the mTOR complexes 1/2 (mTORC1/2) exerts cytostatic effects on tumor cells, the treatment is transient and not curative (Barrera et al., 2013; Davies et al., 2011; Yao et al., 2014), causing recurrence of tumors upon cessation of therapy (Bee et al., 2018; McCormack et al., 2011). This limitation in the therapeutic effects of mTOR pathway inhibitors could well be due to the fact that many patient tumors do not exhibit *TSC* mutations (Beauchamp et al., 1998; Niida et al., 1999, 2001) and express the tuberin protein (Badri et al., 2013; Johnson et al., 2002). Given the debilitating phenotypes in multiple organs resulting in poor clinical outcomes, it is imperative we urgently resolve the source of pathogenic cells in TS. Not only will such knowledge foster the development of more effective treatment and prophylaxis for TS, providing relief to over 2 million sufferers worldwide (Kingswood et al., 2016), understanding the origin of TS lesions and tumors will clarify the sporadic and unpredictable nature of disease pathogenesis. Currently, the precise identification of the source of pathogenic cells in TS remains unclear (Henske et al., 2016; Henske and McCormack, 2012; Lam et al., 2018).

Histologically, TS neoplasms commonly comprise immature cells exhibiting either neuronal characteristic, as found in cortical tubers, subependymal giant giant-cell astroocytomas, and retinal astrocytic hamartomas, and non-neuronal phenotypes found mostly outside of central nervous system (CNS) organs (Brigo et al., 2018; Delaney et al., 2014; Feliciano, 2020). While evidence supporting the postulate that CNS lesions originate due to mTOR-induced neural dysplasia, hyperexcitability, abnormal differentiation, and defective maturation of neural progenitor cells during embryonic development is quite compelling (Feliciano et al., 2012; Lin et al., 2016; Park et al., 2018), the ontogenetic mechanisms of non-CNS lesions of TS is

[1]Center for LAM and Rare Lung Disease, Department of Anesthesiology, College of Physicians and Surgeons, Columbia University, 630 West 168th Street, New York, NY 10032, USA

[2]Department of Pathology, International University of Health and Welfare, School of Medicine, 4-3 Kouzunomori, Narita-shi, Chiba 286-8686, Japan

[3]Department of Biochemistry, Rutgers-Robert Wood Johnson Medical School, Rutgers University, 675 Hoes Lane, Piscataway, NJ 08854, USA

[4]Lead contact

*Correspondence: jmd12@cumc.columbia.edu

https://doi.org/10.1016/j.isci.2021.102684

not well understood. For instance, some research groups have recently made strides to identify the potential origin of the TS neoplastic cells outside the CNS albeit non-concordant findings, including the hypotheses that lymphangioleiomyomatosis (LAM), the main pulmonary manifestation of TS, is caused by cells of a pleural mesothelial origin (Clements et al., 2020) or uterine origin (Guo et al., 2020). Similarly, postulates of a neural crest origin for renal angiomyolipomas (AMLs), the most common cause of mortality in adult TS (Lam et al., 2018), and patients with LAM have been proposed by others. These investigators have observed that lesions in LAM and renal AMLs comprise heterogeneous cells including those that consistently express markers of smooth muscle cells (α-SMA, vimentin, and desmin), melanocytes (HMB45, MART-1), and adipocytes (AdPLA2) (Taveira-DaSilva and Moss, 2015), cell types that are phenotypically mesenchymal and in most cases foreign to their host tissue interstitium (Henske and McCormack, 2012). Coupled with the multi-organ occurrence of TS lesions (Delaney et al., 2014; Henske and McCormack, 2012), the pathogenesis of LAM and non-CNS lesions in TS seems reminiscent of developmental paradigms of neural crest lineages that give rise to portions of the embryonic mesenchyme either as trunk neural crest cells (TNCCs), cranial neural crest cells (CNCC), and cardiac or vagal neural crest cells (NCCs) (Baggiolini et al., 2015). These neural crest subtypes are postulated to determine TS disease heterogeneity (Delaney et al., 2014; Henske and McCormack, 2012), and the timing of *Tsc1/2* mutations in these cells during embryogenesis is predicted to govern the severity of the TS and LAM phenotype (Delaney et al., 2014). However, no experimental data exist to support the hypothesis which remains to be directly and comprehensively investigated (Delaney et al., 2014). Cumulatively, these studies do suggest that TS neoplasms have an embryogenic origin.

Given the relatively high frequency of renal lesions in TS, TS-associated lymphangioleiomyomatosis (TS-LAM), and sporadic LAM (S-LAM) (Dixon et al., 2011; Rakowski et al., 2006; Siroky et al., 2011), we employed a tuberous sclerosis $Tsc2^{+/-}$ reporter mouse model that spontaneously develops renal cystadenomas (Onda et al., 1999) to test the hypothesis that mouse renal neoplasms are neurocristopathies, pathologies borne of a neural crest lineage. The expression of the tdTomato (*TdT*) reporter gene in these mice is governed by a Cre-recombinase-driven event under the control of the myelin protein zero *(Mpz)* promoter, a neural crest lineage marker (Yamauchi et al., 1999). This enables tissues derived from the neural crest to be detected in these mice and pathogenic cells of neural crest lineage to be determined and tracked in growing tumors of the tuberous sclerosis mice and in postmortem biochemical analyses. *Mpz* expression has previously been associated with multipotent post-migratory differentiating neural crest progenitors that exhibit fate restrictions including smooth muscle-like cells, glia, and neurons dependent on the cellular context and instructive environmental cues (Dupin and Coelho-Aguiar, 2013; Hagedorn et al., 1999). HMB45-positive angiomyolipoma and cystic single cells have also been identified in otherwise normal renal parenchyma (Siroky et al., 2011) reminiscent of migratory pathogenic neural crest-derived cells that defines our hypothesis (Pacheco-Rodriguez and Moss, 2010). The slow development of these tumors in the heterozygote *Tsc2* mice (Kwiatkowski, 2010; Onda et al., 1999) mimics the gradual benign growth pattern of TS hamartomas in most patients making this mouse model a suitable translational animal model for this study.

Using a non-invasive imaging strategy comprising epifluorescent IVIS spectral imaging and small animal ultrasound, we report the earliest detection of ectopic renal neoplasms in these tuberous sclerosis mice at 4 months of age. We resolved that a small population of primitive neural crest precursors, whose number increases with increasing tumor volume and maturity, populates renal tumors in the tuberous sclerosis mice and could source renal tumor ontogenesis in TS.

RESULTS

Generation of the tuberous sclerosis reporter mouse model

To determine whether TS tumor cells originate from a neural crest lineage, we generated a recapitulative mouse model by crossing floxed B6.Cg-Gt(ROSA)26Sor$^{tm9(CAG\text{-}tdTomato)Hze}$/J reporter mice with transgenic B6N.FVB-Tg(Mpz-Cre)26Mes/J mice. Using genotyping studies, we next selected *Mpz(Cre)/TdT*$^{fl/fl}$ reporter mice progeny expressing TdT driven by the myelin protein zero promoter (*Mpz*) (Yamauchi et al., 1999). Upon breeding these mice with the $Tsc2^{+/-}$ tuberous sclerosis mice (Onda et al., 1999) and F1 hybrid crosses of resulting $Tsc2^{+/-}$/*Mpz(Cre)*/TdT$^{fl/+}$ progeny, experimental mice denoting genotypes $Tsc2^{+/-}$/*Mpz(Cre)*/TdT$^{fl/fl}$, $Tsc2^{+/-}$/*Mpz(Cre)*/TdT$^{+/+}$, $Tsc2^{+/+}$/*Mpz(Cre)*/TdT$^{fl/fl}$, and wild-type control $Tsc2^{+/+}$/*Mpz(Cre)*/TdT$^{+/+}$ mice were aged for 16 months to allow for tumor development. A schematic of genetic crosses involved in the development of this mouse model is displayed in Figure 1A. These crossings generate an animal model that allows for systemic epifluorescent detection of neural crest lineage cells in developing TS

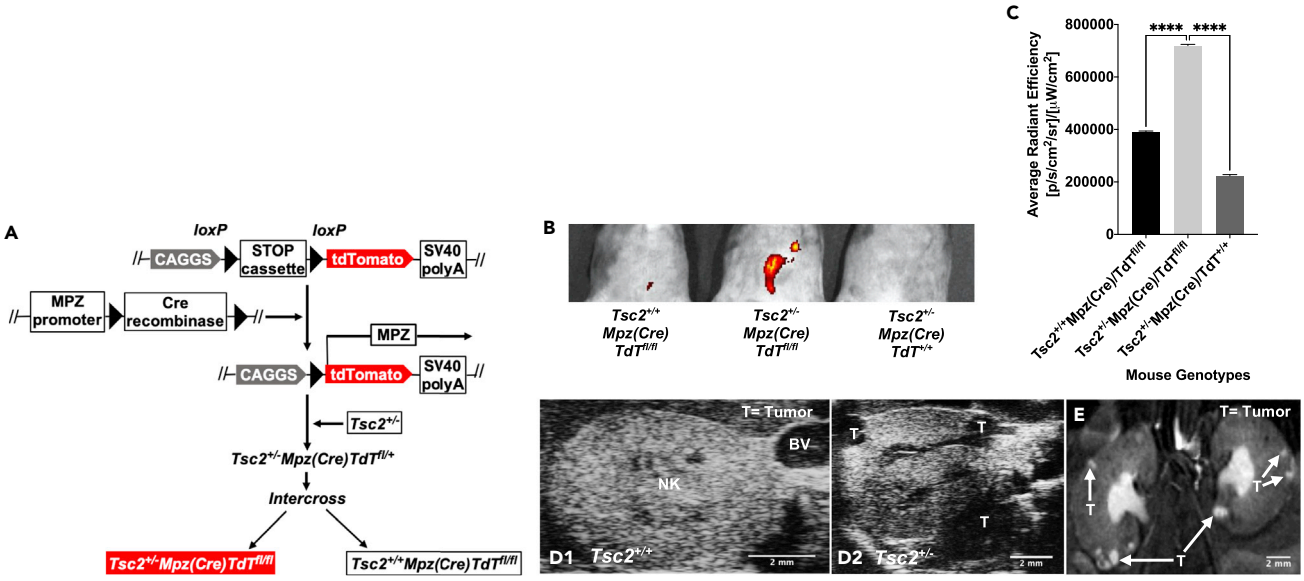

Figure 1. Generation of tuberous sclerosis reporter mouse model

(A) Schematic of genetic crosses to generate *Tsc2*$^{+/-}$ reporter mouse models shows floxed *R26Sor*$^{tm9(CAG\text{-}tdTomato)Hze}$ mice (female, N = 10 animals) were crossed with Tg(Mpz-Cre)26Mes mice (male, N = 10 animals) expressing Cre recombinase under the control of myelin protein zero (*Mpz*) promoter. Mice with *Mpz(Cre)* $^{tm1.1JDar}$ mouse progeny (male/female, N = 8 animals) were then mated with *Tsc2*$^{+/-}$ mice (male/female, N = 10 animals) to source *Tsc2*$^{+/-}$/*Mpz(Cre)*/TdT$^{fl/fl}$ tuberous sclerosis reporter mouse models (shown in red) (male/female, N = 24 animals) that spontaneously develop renal tumors driven by neural crest cells labeled with tdTomato.

(B) IVIS spectral images of abdominopelvic cavities of 1.3-yr-old *Tsc2*$^{+/-}$/*Mpz(Cre)*/TdT$^{fl/fl}$ tuberous sclerosis mouse model compared to age-matched *Tsc2*$^{+/-}$*Mpz(Cre)TdT*$^{+/+}$ and *Tsc2*$^{+/+}$*Mpz(Cre)TdT*$^{fl/fl}$ mice distinguishing epifluorescence of tdTomato-expressing regions.

(C) Average radiant efficiency was used to compare tdTomato epifluorescence in these mouse models by one-way analysis of variance (ANOVA) and post-hoc Dunnett's test ($p < 0.0001$****). Small animal ultrasound scans of sagittal sections of normal kidney (NK) parenchyma in adult wild-type mice imaged on a viewing stage in supine position (D1) in comparison to renal sagittal sections in *Tsc2*$^{+/-}$*Mpz(Cre)TdT*$^{fl/fl}$ mice (D2) with labeled sites of tumors (T). BV denotes blood vessels. Rapid magnetic resonance images of kidneys (E) in *Tsc2*$^{+/-}$*Mpz(Cre)TdT*$^{fl/fl}$ mice identifying tumors (T) shown with arrows. See also Figures S1A–S1C comparing ultrasound and MRI images of tumorigenic hepatic tissues in *Tsc2*$^{+/-}$*Mpz(Cre)/TdT*$^{fl/fl}$ mice to normal liver tissue of *Tsc2*$^{+/+}$*Mpz(Cre)/TdT*$^{fl/fl}$ mice.

tumors by Cre-recombinase-mediated insertion of the *Mpz* promoter to drive tdTomato expression (Liu et al., 2015; Yamauchi et al., 1999). Tumor tracking in this *Tsc2*$^{+/-}$ reporter mice was performed beginning at 2 months of age at biweekly intervals using sequential In Vivo Imaging System (IVIS) spectral imaging detecting tdTomato excitation/emission spectra at 570 nm/620 nm and small animal ultrasound. Small animal magnetic resonance imaging was used to confirm sites of tumor development prior to excision for subsequent analysis. Figure 1B displays results of IVIS spectral imaging of an array of 16-month-old littermate progeny of the selected genotypes used in this study showing tdTomato epifluorescence to be perceptibly brightest in the abdominal region of only the *Tsc2*$^{+/-}$/*Mpz(Cre)*/TdT$^{fl/fl}$ mice. Spectral quantification of tdTomato epifluorescence revealed significantly higher average radiant efficiency measurements ($p < 0.0001$***) in *Tsc2*$^{+/-}$/*Mpz(Cre)*/TdT$^{fl/fl}$ mice compared to other mouse genotypes in two different sets of mice imaging studies (Figure 1C). TS tumorigenesis in this select mouse group was further verified by ultrasound imaging resolving regions representing multiple peripheral tumors in the kidneys of *Tsc2*$^{+/-}$/*Mpz(Cre)*/TdT$^{fl/fl}$ mice (Figure D2) compared to tumor-less renal tissue in the *Tsc2*$^{+/+}$/*Mpz(Cre)*/TdT$^{fl/fl}$ mice (Figure D1). High-resolution magnetic resonance imaging confirmed the presence of bilateral cortical tumor growth in both kidneys of the *Tsc2*$^{+/-}$/*Mpz(Cre)*/TdT$^{fl/fl}$ mice (Figure 1E). *Tsc2*$^{+/-}$/*Mpz(Cre)*/TdT$^{+/+}$ mice spontaneously developed renal tumors which could not be detected by tdTomato epifluorescence. Hepatic lesions were also detected in the 16-month-old *Tsc2*$^{+/-}$/*Mpz(Cre)*/TdT$^{fl/fl}$ mice by ultrasound imaging (Figure S1B) compared to cross-sectional images of non-tumorigenic hepatic tissues recovered from *Tsc2*$^{+/+}$/*Mpz(Cre)*/TdT$^{fl/fl}$ mice (Figure S1A). The presence of hepatic lesions in the *Tsc2*$^{+/-}$/*Mpz(Cre)*/TdT$^{fl/fl}$ mice was further confirmed by high-resolution MRI (Figure S1C).

Renal tumorigenesis in Tsc2$^{+/-}$ mice correlates with onset and proliferation of neural crest precursor populations

Prior to our study, the earliest reported detection of renal neoplasms in tuberous sclerosis *Tsc2*$^{+/-}$ mouse models was at 6 months of age (Kobayashi et al., 1999; Kwiatkowski, 2010; Lam et al., 2018; Onda et al.,

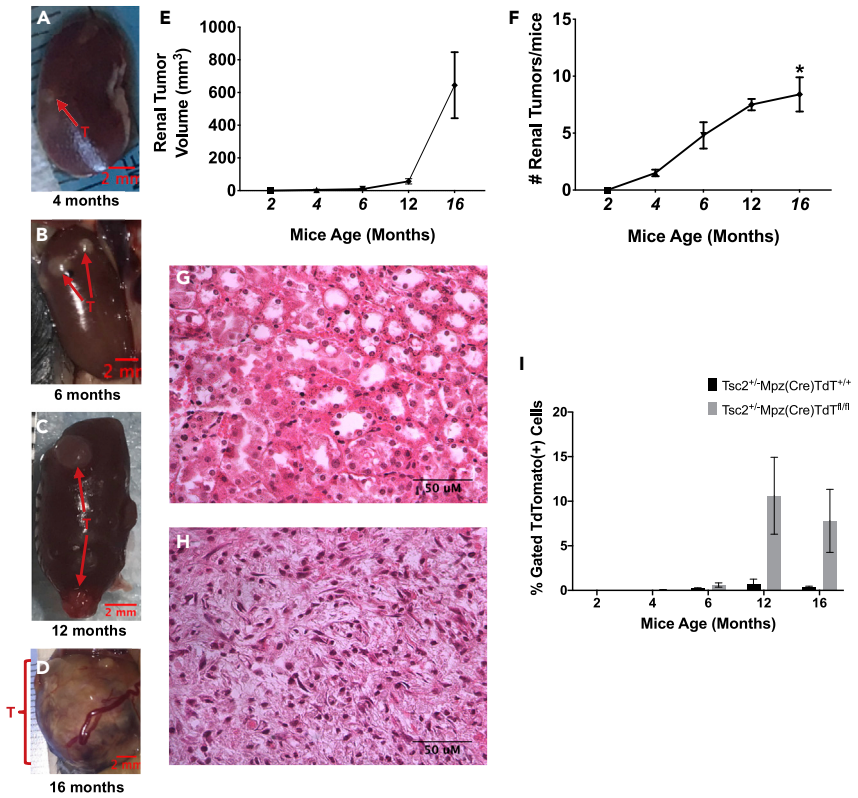

Figure 2. Renal tumorigenesis in *Tsc2*$^{+/-}$ mice correlates with onset and proliferation of neural crest precursor populations

(A–D) Earliest reported detection of ectopic renal tumors in the *Tsc2*$^{+/-}$*Mpz(Cre)TdT*$^{fl/fl}$ mice at 4 months of age (A), then pictured at 6 months (B), 12 months (C), and 16 months (D).

(E) Tumor volume increased from 4.68 ± 1.5 mm^3 at 4 months of age (male/female, N = 5 animals) to 9.66 ± 1.9 mm^3 at 6 months (male/female, N = 6 animals), to 56.8 ± 16.0 mm^3 at 12 months (male/female, N = 5 animals), and then increasing by over 1,100% to 645 ± 202 mm^3 by 16 months of age (male/female, N = 6 animals).

(F–H) (F) The average number of tumors per mice increased proportionally during the same period from 1.50 ± 0.3 (N = 5 animals; p = 0.895) in 4-month-old mice, to 4.80 ± 2.6 (N = 6 animals) in 6-month-old mice, and 7.50 ± 0.7 (N = 5 animals; p = 0.068) in 12-month-old mice, reaching statistical significance in 16-month-old mice (8.40 ± 3.4; *p = 0.025; N = 6 animals) compared to the 2-month-old mice. Representative images of hematoxylin/eosin (H/E)-stained immunohistochemical slides of renal tissue cross sections (4μM thickness) from 12-month-old *Tsc2*$^{+/+}$*/Mpz(Cre)*/TdT$^{fl/fl}$ mice (G) and *Tsc2*$^{+/-}$*/Mpz(Cre)*/TdT$^{fl/fl}$ mice (H).

(I) Renal tumors from 4- to 16-month-old *Tsc2*$^{+/-}$ *Mpz(Cre)TdT*$^{fl/fl}$ mice were dissociated, gated for live/dead staining (Sytox Green$^{(-)}$/DAPI$^{(-)}$/DRAQ5$^{(+)}$), and sorted for tdTomato expression in comparison with renal cortical cells obtained from age-matched *Tsc2*$^{+/+}$ *Mpz(Cre)TdT*$^{fl/fl}$ mice.

1999), and earlier polycystic lesions occurring in the *Dermo1*^{Cre};*Tsc2*$^{fl/fl}$ mice led to mouse lethality by 3 weeks of age (Ren et al., 2016). We report the earliest detection of ectopic fluid-filled renal cysts spontaneously developing in *Tsc2*$^{+/-}$*/Mpz(Cre)*/TdT$^{fl/fl}$ by 4 months of age (Figure 2A). These tumors were detectable by both IVIS spectral imaging and ultrasound. By 6 months of age, multiple solid tumors and/or cysts containing denser fluid can be observed (Figure 2B), which increased in volume by 12 months (Figure 2C), and by 16 months, enlarged, dysmorphic, inflamed renal tissue coalescing with multiple cysts could be observed (Figure 2D). Individual renal tumor volumes varied widely within the same kidney and mice at all ages, doubling in the mean volume from 4.68 ± 1.5 mm^3 at 4 months of age (N = 4 mice) to 9.66 ± 1.9 mm^3 at 6 months (N = 5 mice), to 56.8 ± 16.0 mm^3 at 12 months (N = 3 mice), and then increasing by over 1,100% to 645 ± 202 mm^3 by 16 months of age (Figure 2E). The average number of renal tumors per mice increased from 1.50 ± 0.3 (N = 4 mice; p = 0.895) in 4-month-old mice, to 4.80 ± 2.6 (N = 5 mice; p = 0.213) in 6-month-old mice, and to 7.50 ± 0.7 (N = 3 mice; p = 0.068) in 12-month-old mice, reaching statistical significance in 16-month-old mice (8.40 ± 3.4 tumors; N = 5 mice; *p = 0.025) compared to the 2-month-old mice (Figure 2F).

Tsc2$^{+/-}$ mice renal tumors and comparative renal cortical tissues were excised at 4, 6, 12, and 16 months. Representative images of hematoxylin/eosin (H/E)-stained immunohistochemical slides of renal tissue cross sections (4 μM thickness) from 12-month-old *Tsc2*$^{+/+}$/*Mpz(Cre)*/TdT$^{fl/fl}$ mice (Figure 2G) and *Tsc2*$^{+/-}$/*Mpz(Cre)*/TdT$^{fl/fl}$ mice (Figure 2H) are depicted. *Tsc2*$^{+/-}$ reporter mice renal tissues and tumors were dissociated into single cell populations for flow cytometric sorting of tdTomato^{+} NCCs. Results indicate that the significant increase in renal tumor volume (Figure 2E) and number of tumors (Figure 2F) in *Tsc2*$^{+/-}$/*Mpz(Cre)*/TdT$^{fl/fl}$ mice over the 16-month-period correlated with a marked increase in the fraction of gated tdTomato^{+} cells from an average of 0.60% beginning at 6 months, to 10.6% at 12 months, and 7.8% of the total number of sorted cells at 16 months (Figure 2I) compared to sorted cell fractions from *Tsc2*$^{+/+}$/*Mpz(Cre)*/TdT$^{fl/fl}$ mice and *Tsc2*$^{+/-}$/*Mpz(Cre)*/*TdT*$^{+/+}$ following gating protocols for live cells (DAPI$^{(-)}$/Sytox Green$^{(-)}$/DRAQ5$^{(+)}$) and tdTomato$^{(+)}$. Representative dot plots comparing gating results of flow cytometric separation of renal tissue and tumor cells between *Tsc2*$^{+/+}$/*Mpz(Cre)*/TdT$^{fl/fl}$ and *Tsc2*$^{+/-}$/*Mpz(Cre)*/TdT$^{fl/fl}$ obtained at 4 months (Figures 3A and 3B), 6 months (Figures 3C and 3D), 12 months (Figures 3E and 3F), and 16 months (Figures 3G and 3H), respectively, are also displayed. Single cell suspensions of CNCCs (Figure 3I) and TNCCs (Figure 3J) excised from 9.5dpc *Tsc2*$^{+/-}$*Mpz(Cre)TdT*$^{fl/fl}$ mice embryos were used as positive controls to comparatively assess the emergence of tdTomato^{+} NCCs in tuberous sclerosis *Tsc2*$^{+/-}$ mice. The resolution of tdTomato^{+} cells in renal tumor cell dissociates indicates active *Mpz* promoter activity in cells of a neural crest lineage. This unique cell population likely results from migrants from the neural crest that retain their proliferative and stem cell character and differentiate into source pathogenic tumor cells of TS, as phenotypic manifestations of mono-allelic and biallelic mutations at the *Tsc2* gene locus. Although the fraction of these tdTomato-expressing cells in both the gated and whole-cell populations analyzed by flow cytometry is quite low, they are proportional in quantity to the NCC precursors recoverable from 9.5dpc embryonic cranial tissue and mesodermal somite used as our cranial and trunk NCC controls, respectively (Figures 3I and 3J).

Characterization of neural crest lineage cells in Tsc2$^{+/-}$ mouse renal tumors

Immunohistochemical preparations of excised renal tumor slices (4 μm thickness) obtained from 6-month-old *Tsc2*$^{+/-}$/*Mpz(Cre)*/TdT$^{fl/fl}$ mice revealed red fluorescent punctate cell masses occurring singly or in small colonies in the renal tumor slices following fluorescence excitation using the Texas Red chromatic filter (Figures 4A and 4B). The proportion of red fluorescent cells in renal tumors increased with age where even more colonies can be seen in the 12-month-old *Tsc2*$^{+/-}$/*Mpz(Cre)*/TdT$^{fl/fl}$ mouse tumor slices (Figures 4C and 4D) and 16-month-old *Tsc2*$^{+/-}$/*Mpz(Cre)*/TdT$^{fl/fl}$ mouse tumor slices (Figures 4F–4H) compared to renal tissue wildtype at the *Tsc2* locus (Figure 4E). Double immunolabeling studies using the 16-month-old renal tumor slices reveal significant expression of neural crest marker CD57 (β-1,3-glucuronyltransferase (B3GAT1)) in select renal tumor cells by confocal microscopy, along with 4′,6-diamidino-2-phenylindole (DAPI) nuclear staining and endogenous tdTomato expression reporting the tumor's neural crest phenotype (Figure 3H). These tdTomato^{+} cell masses were also observed in hepatic tumor slices obtained from *Tsc2*$^{+/-}$/*Mpz(Cre)*/TdT$^{fl/fl}$ mice (Figures S1D and S1E). The myelin protein zero (*Mpz*)-driven tdTomato expression of cells in renal and hepatic tumors of the *Tsc2*$^{+/-}$ reporter mice is a direct demonstration of a neural crest lineage for these tumors. Although we have not yet successfully extracted sufficient reliable genomic and proteomic material from tdTomato^{+} flow-sorted cells for downstream applications in this pilot study, RT-qPCR analysis of excised whole renal tumors from *Tsc2*$^{+/-}$*Mpz(Cre)TdT*$^{fl/fl}$ mice compared to age-matched *Tsc2*$^{+/+}$/*Mpz(Cre)TdT*$^{fl/fl}$ mice renal tissue exhibited significantly higher expression of select neural crest markers *Ap2α* ($p = 4.40 \times 10^{-3}$**) and *CD57* ($p = 0.05$*) (Figure 5A) in renal tumors assessed including *Tsc2*-null and *Tsc2*-expressing mouse renal tumors. In aggregate, *Tsc2*$^{+/-}$ mice renal tumors assessed in this study did not exhibit significantly different *Tsc2* gene expression compared to renal cortical tissues in normal mice ($p = 0.0824$) (Figure 5B) in concordance with findings from our previous studies using this mouse model (D'Armiento et al., 2016).

DISCUSSION

The present study demonstrates through lineage tracing that renal angiomyolipomas and hepatic tumors in *Tsc2*$^{+/-}$ reporter mouse models harbor NCCs. The occurrence of this population of NCCs was confirmed using fluorescent and confocal microscopy, flow cytometric analyses, and immunohistochemistry, substantiating the lineage tracing results. The lineage tracing studies utilizing the myelin protein zero (*Mpz)* promoter, therefore, are representative of expression of the ectodermal neural crest. The immunologic expression of canonical neural crest marker *CD57* in tdTomato-positive renal tumor cells (Figure 3H) further confirms their neural crest cellular identity, as well as the differential expression of multiple neural crest

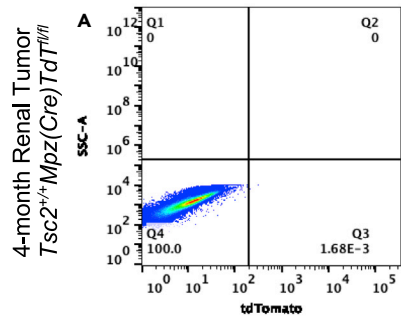

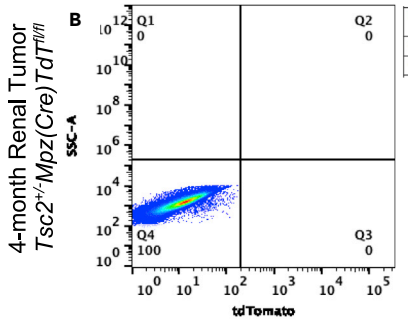

Sample Name	Q3 Cell Count	Freq. of Parent (%)	Freq. of Total (%)
4-month *Tsc2+/+Mpz(Cre)TdTfl/fl*	0	0.00168	0.000198
4-month *Tsc2+/-Mpz(Cre)TdTfl/fl*	0	0	0

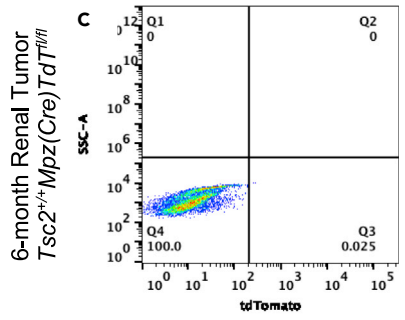

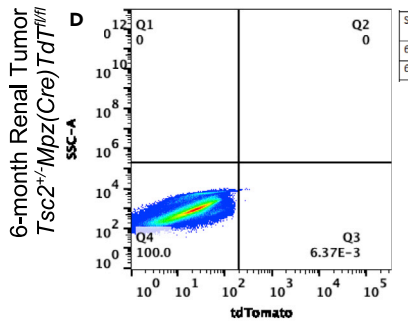

Sample Name	Q3 Cell Count	Freq. of Parent (%)	Freq. of Total (%)
6-month *Tsc2+/+Mpz(Cre)TdTfl/fl*	2	0.025	0.002
6-month *Tsc2+/-Mpz(Cre)TdTfl/fl*	11	0.00637	0.0005

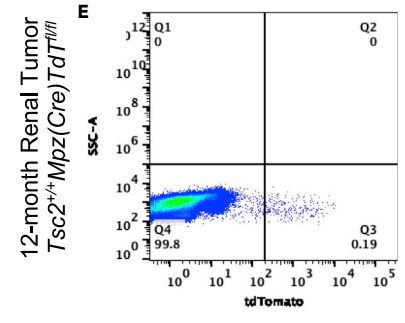

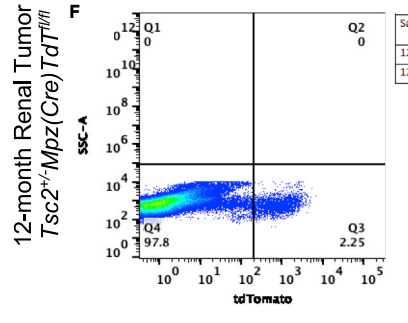

Sample Name	Q3 Cell Count	Freq. of Parent (%)	Freq. of Total (%)
12-month *Tsc2+/+Mpz(Cre)TdTfl/fl*	248	0.19	0.015
12-month *Tsc2+/-Mpz(Cre)TdTfl/fl*	2809	2.25	0.2

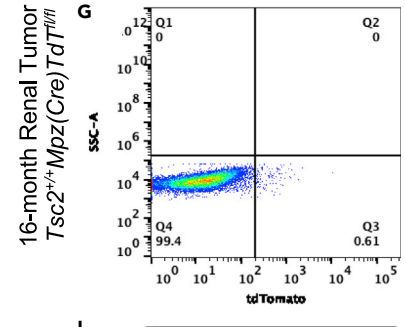

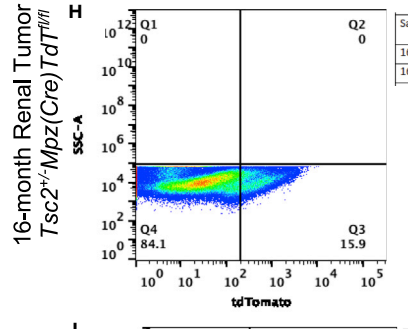

Sample Name	Q3 Cell Count	Freq. of Parent (%)	Freq. of Total (%)
16-month *Tsc2+/+Mpz(Cre)TdTfl/fl*	118	0.61	0.15
16-month *Tsc2+/-Mpz(Cre)TdTfl/fl*	19839	15.9	6.45

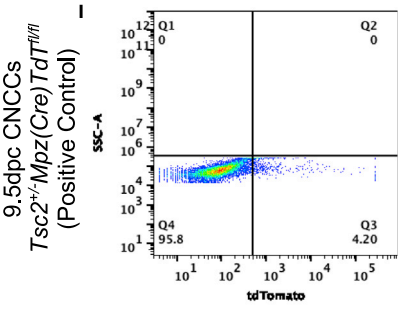

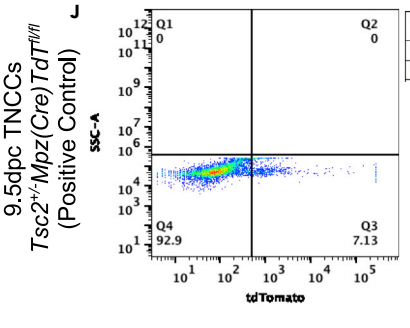

Sample Name	Q3 Cell Count	Freq. of Parent (%)	Freq. of Total (%)
9.5dpc *Tsc2+/-Mpz(Cre)TdTfl/fl* CNCC	461	4.2	1.2
9.5dpc *Tsc2+/-Mpz(Cre)TdTfl/fl* TNCC	547	7.13	1.09

Figure 3. Flow cytometric analysis of tdTomato-positive neural crest precursors in *Tsc2*$^{+/-}$ reporter mice renal tumors

Representative flow cytometric data comparing single-cell events obtained between renal cortical tissue of *Tsc2*$^{+/+}$ *Mpz(Cre)TdT*$^{fl/fl}$ mice and *Tsc2*$^{+/-}$ *Mpz(Cre)TdT*$^{fl/fl}$ reporter mice at 4 months (A and B), 6 months (C and D), 12 months (E and F), and 16 months (G and H) are displayed, respectively. Single-cell suspensions of cranial neural crest cells (CNCCs) (I) and trunk neural crest cells (TNCCs) (J) excised from the 9.5dpc *Tsc2*$^{+/-}$*Mpz(Cre)TdT*$^{fl/fl}$ mice embryos were used as positive controls to assess the emergence of tdTomato^{+} neural crest cells in tuberous sclerosis mice. Flow cytometric data shown is one representative experiment of doublet studies performed at different times using N = 2-3 mice/genotype/age group/experiment. Acquisition and analyses of flow cytometric data was performed on a Bio-Rad S3e cell sorter and analyzed using FlowJo 10.7.1/FCS Express 7 Plus software. All statistics were performed using a one-way ANOVA with post-hoc Dunnett test for multiple comparisons.

markers in diseased mouse renal tumors compared to healthy kidney tissues. The multipotency demonstrated by the expression pattern suggests that the tumor cell subpopulations are migrant neural crest progenitor relics of neurocristogenesis that have co-opted tumorigenesis in their various domiciled organs. Interestingly, the NCCs increased in number as the mice aged and the tumors increased in size. The described findings potentially allow for the development of efficacious targeted therapy for this untreated rare disease.

It is well established that neural crest progenitor cells are destined to delaminate from the neural tube, undergo epithelial-mesenchymal transitions (EMT), and invade multiple organs to give rise to CNCCs and trunk and vagal NCCs (Minarcik and Golden, 2003; Osumi-Yamashita et al., 1994; Serbedzija et al., 1992). NCCs are variably lineage restrictive in their multipotency, maintaining their ability to differentiate into few or many different cell types (Achilleos and Trainor, 2012; Baroffio et al., 1991; Calloni et al., 2009; Krispin et al., 2010; Motohashi et al., 2011), while retaining their multipotent self-renewal capacity even into adulthood in mammals (Bhatt et al., 2013). Interestingly, these cytogenetic activities mimic routine tumor cell physiology with ample evidence existing to demonstrate that cancer cells co-opt many of the genetic and molecular mechanisms used by developing NCCs including EMT, proliferation, migration, and differentiation (Maguire et al., 2015). Furthermore, the fate of these migratory and post-migratory NCCs is not completely determined, even after domiciliation in target organs, because they continue to generate multiple tissue derivatives (Maguire et al., 2015). The predilection of renal neoplasms in the *Tsc2*$^{+/-}$ mice and in most patients with TS could well be due to these embryogenetic lineage restrictions in the tumorigenic *Tsc2*$^{+/-}$ NCC subpopulations. Additionally, renal organs could also possess the most conducive microenvironment to co-opting tumorigenesis in these cells due to the presence of activating factors such as hormone stimulation (Yu et al., 2009).

The findings from the foregoing studies present a number of interesting possibilities. Given the embryonic nature of NCCs, it can be assumed that tumors in the tuberous sclerosis *Tsc2*$^{+/-}$ mouse model harbor NCCs possessing mono-allelic germline mutations at the *Tsc2* gene loci. As haploinsufficient TS mutations have been shown to suffice for TS and LAM pathogenicity similar to *Tsc2*$^{-/-}$ neoplastic cells (D'Armiento et al., 2016; Julian et al., 2017; Martin et al., 2017; Peri et al., 2017; Tam et al., 2019), multipotent *Tsc2*$^{+/-}$ NCCs could induce tumor development in both ectodermally-derived neural and non-neural tissues (Feliciano, 2020; Ferrans et al., 2000) located in multiple organs that are ontogenetic destinations for neural crest progenitor cells (Delaney et al., 2014). Supporting this postulate is the recent delineation of catabolic signaling potentially inducing mesenchymal lineage specificity in human pluripotent stem cell-derived NCCs upon complete ablation of *Tsc2* expression (Delaney et al., 2020). Similarly, *Tsc1*$^{-/-}$ NCCs were observed to drive the development of sclerotic craniofacial bone lesions in a floxed *Tsc1*$^{-/-}$*/Mpz* mouse model (Fang et al., 2015). Furthermore, concomitant increase in tumor volume and number with increases in the proportion of tdTomato^{+} NCCs identified in this study could indicate that more *Tsc2*$^{+/-}$ NCCs initiate increased interstitial paracrine signaling that thus co-opt a greater number of host cells expanding proliferation and secretion of cystic volume. More tdTomato^{+} NCCs engaging in self-renewal proliferative processes can account for large numbers of tumors in the same or varied organs which altogether index more aggressive tumorigenic phenotypes.

Mutations in the *Tsc1* and predominantly the *Tsc2* gene loci give rise to constitutive mTOR kinase activity and unregulated cell growth and metabolism causing TS tumors (El-Hashemite et al., 2003; Giannikou et al., 2016; Inoki et al., 2003; Kenerson et al., 2007). However, in studies conducted by our group and others (Hartman et al., 2009; Higa et al., 2009; Lee et al., 2010; Li et al., 2014), several mTOR-independent pathogenic mechanisms for TS have been demonstrated in diseased tissues haploinsufficient at the *Tsc2* locus. Such exemplary mTOR-independent signaling was observed in our studies demonstrating the requirement of the misexpression of DNA transcription factor High-Mobility Group (*Hmga2*) in mesenchymal and

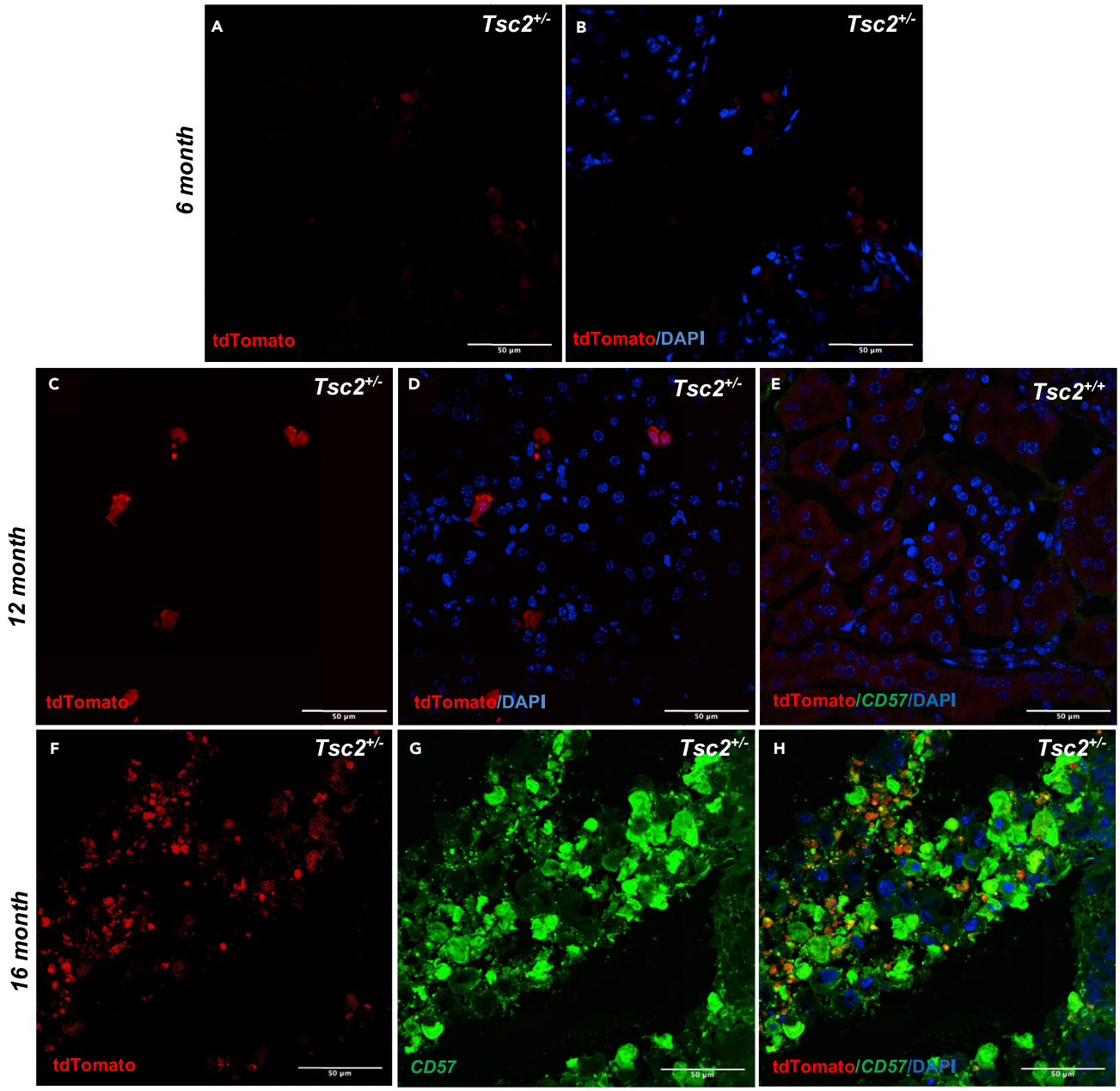

Figure 4. Visualizing neural crest lineage cells in *Tsc2*$^{+/-}$ mouse renal tumors

(A–D) Representative tdTomato and merged tdTomato/DAPI images of immunohistochemical slices (4 μM thickness) of renal tumors showing punctate singlets and colonies of tdTomato^{+} neural crest cell populations obtained in 6-month-old (A and B) and 12-month-old (C and D) *Tsc2*$^{+/-}$*Mpz(Cre)TdT*$^{fl/fl}$ mice viewed using an excitation filter of 540/45 nm in a confocal microscope.

(E–H) (E) Comparative image panel of renal tissue from wild-type 12-month-old mice. Double immunolabeling of renal tumor slices obtained from 16-month-old *Tsc2*$^{+/-}$*Mpz(Cre)TdT*$^{fl/fl}$ mice reveal tandem endogenous expression of *Mpz*-driven tdTomato red fluorescent protein (F), Alexa Fluor 488-labeled CD57 neural crest marker expression (G), and tdTomato/CD57/DAPI merged images (H) confirming neural crest identity of these cells. Confocal and fluorescence imaging was performed using N = 3 slides; 2 sections/slide to visualize each renal tumor/tissue. Scale bar represents 50μm. See also Figures S1D and S1E for fluorescent imaging of immunohistochemical slices of hepatic lesions of *Tsc2*$^{+/-}$*Mpz(Cre)/TdT*$^{fl/fl}$ mice showing punctate tdTomato^{+} NCCs.

epithelial tumors, and the concomitant expression of upstream and downstream targets of *Hmga2* such as insulin-like growth factor 2 mRNA-binding protein 2 *(Igf2bp2)*, *let-7*, and *lin28* in *Tsc2*$^{+/-}$ mouse tumors (Berner et al., 1997; D'Armiento et al., 2007; D'Armiento et al., 2016; Hunter et al., 2002; Kazmierczak et al., 1996; Tallini et al., 2000). This implicates an active Hmga2 pathway inducing tumorigenesis in these

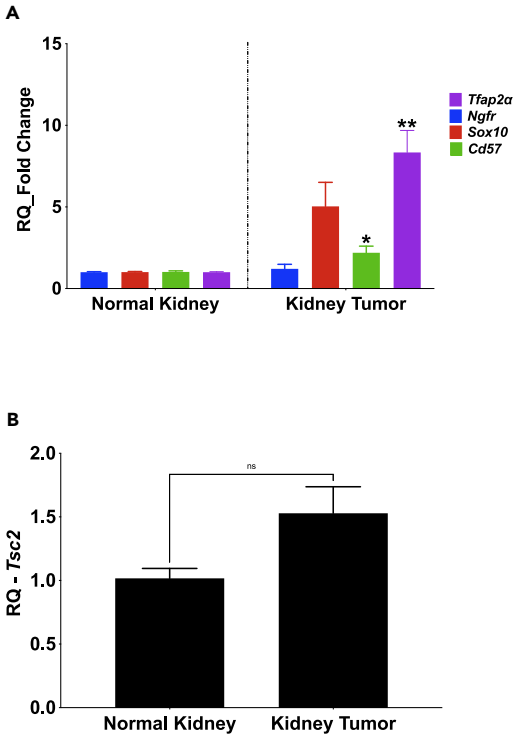

Figure 5. Neural crest marker expression in *Tsc2*$^{+/-}$ mouse renal tumors

(A) RNA extracts of *Tsc2*$^{+/+}$*Mpz(Cre)TdT*$^{fl/fl}$ mice kidney parenchyma and *Tsc2*$^{+/-}$*Mpz(Cre)TdT*$^{fl/fl}$ mice renal tumors from 16-month-old mice analyzed by RT-qPCR for neural crest marker expression depict significantly increased expression of transcription factor activating protein—*Tfap2α* ($p = 4.40 \times 10^{-3}$**) and *CD57* (β-1,3-glucuronyltransferase (B3GAT1)) ($p = 0.05$*).

(B) There was no statistically significant difference in *Tsc2* gene expression state between wild-type kidney tissues and renal tumors in *Tsc2*$^{+/-}$ mice ($p = 0.0824$). RT-qPCR experiments were performed using triplicate biological samples applied in PCR plates in quadruplicates.

study models. Given our findings and above that TS tumors are phenotypically mesenchymal and originate from the neural crest and the exclusive expression of *Hmga2* in embryonic undifferentiated mesenchyme (Chiappetta et al., 1996; Hock et al., 2006), *Hmga2* misexpression could potentially define the ability of *Tsc2*$^{+/-}$ NCCs to form mesenchymal tumors. Furthermore, it is evident that the pathogenic cells of TS possess an enduring stemness characteristic. *HMGA2* as a stemness gene has been implicated in NCC fate specification (Macri et al., 2016) and self-renewal of NCC derivative neural stem cells (Nishino et al., 2008), regulating these developmental events in a manner similar to the gene's effect in propagating mammalian tumorigenesis (Macri et al., 2016; Nishino et al., 2008). NCC progenitors differentiate into ecto-mesenchymal tissue derivatives following EMT during embryogenesis (Duband, 2000; Duband et al., 1995). Given our prior determination of the necessity for expression of *Hmga2* for mesenchymal tumorigenesis in *Tsc2*$^{+/-}$ mice, the gene's expression in 100% of human and mice TS tumors, and its influence in increasing the number of renal tumors (D'Armiento et al., 2016), *Hmga2* could be acting downstream of NCC delamination and *Tsc2* mutational events to determine the tumorigenic potential and destiny of migratory NCCs causative for TS neoplasms.

These studies provide evidence for a neural crest origin for tumorigenic cells in lesions from *Tsc2*$^{+/-}$ mouse models and suggest that a treatment approach specifically targeting neural crest progenitor cells could potentially provide an alternative to mTOR inhibitors as treatment for TS. While mTOR inhibitors remain cytostatic to TS tumorigenic cells (Henske and McCormack, 2012), inhibitors to neural crest markers such as *AP2α* expressed in renal tumors examined in this study have the potential to inhibit DNA transcription and stymy tumor cell growth leading to an alternative or adjunctive therapeutic agent for TS.

Limitations of the study

Given the multi-systemic occurrence of neoplasms in patients with TS as well as in the *Tsc2*$^{+/-}$ reporter mouse model, it would have been prudent to distinguish the genomic characteristic of individual tumors assessed from the same or different diseased mouse organ(s). However, the low proportion and viability of flow-sorted tdTomato+ renal tumor cells resolved in this study limited our ability to perform downstream biochemical analysis of excised tumors, necessitating our pooling of tumors for analysis. This was not an ideal methodology for comprehensive testing of our hypothesis that *Tsc2*$^{+/-}$ mouse renal tumors were neurocristopathic because the characteristic phenotype of these different tumors is thus not known. Future

single-cell RNA sequencing studies of dissociated *Tsc2*$^{+/-}$ mouse renal tumors will overcome this limitation. Additionally, the inability of the majority of *Tsc2*$^{+/-}$ mice to spontaneously develop pulmonary tumors, as well as other regularly occurring tumors and phenotypes of patients with TS, limits its appropriateness as a model of TS and specifically LAM, central to our laboratory investigations. The short life span of the Mpz-driven tdTomato expression in renal tumors limits our ability for prolonged microscopic examination of renal tumor slices by confocal or fluorescence microscopy and employing anti-tdTomato antibodies did not diminish the quenching of the fluorescent signal.

STAR★METHODS

Detailed methods are provided in the online version of this paper and include the following:

- KEY RESOURCES TABLE
- RESOURCE AVAILABILITY
  - Lead contact
  - Materials availability
  - Data and code availability
- EXPERIMENTAL MODEL AND SUBJECT DETAILS
  - Mouse genetic studies
- METHOD DETAILS
  - Tumor tracking protocols
  - Mouse renal tumor processing and flow cytometry
  - Neural crest cell culture
- QUANTIFICATION AND STATISTICAL ANALYSIS

SUPPLEMENTAL INFORMATION

Supplemental information can be found online at https://doi.org/10.1016/j.isci.2021.102684.

ACKNOWLEDGMENTS

We thank Tina Zelonina for assistance in mouse breeding and genotyping, tumor excision, and volume measurements. We also thank Christopher Damoci for his technical expertise during small animal imaging and data analysis. This study was supported by grants from the Center for LAM and Rare Lung Diseases at Columbia University. J.D is supported by NIH RO1-HL086936 and Congressionally Directed Medical Research Programs (CDMRP) grant (TS170057). U.U is supported by Congressionally Directed Medical Research Programs (CDMRP) grant (TS170057). M.G is supported by NIH KO8 (HL126071).

AUTHOR CONTRIBUTIONS

Conceptualization, U.U., T.S., K.C., and J.D.; methodology, U.U., T.S., M.G., and J.D.; investigation, U.U.; formal analysis, U.U.; resources, M.G. and J.D.; writing – original draft, U.U., T.S., and J.D.; writing – review & editing, U.U., M.G., K.C., and J.D.; visualization, U.U. and J.D.; supervision, K.C. and J.D.; funding acquisition, M.G. and J.D.

DECLARATION OF INTERESTS

The authors declare no competing interests.

INCLUSION AND DIVERSITY

We worked to ensure sex balance in the selection of non-human subjects. One or more of the authors of this paper self-identifies as an underrepresented ethnic minority in science. While citing references scientifically relevant for this work, we also actively worked to promote gender balance in our reference list. The author list of this paper includes contributors from the location where the research was conducted who participated in the data collection, design, analysis, and/or interpretation of the work.

Received: December 15, 2020
Revised: April 20, 2021
Accepted: May 31, 2021
Published: July 23, 2021

REFERENCES

Achilleos, A., and Trainor, P.A. (2012). Neural crest stem cells: discovery, properties and potential for therapy. Cell Res. *22*, 288–304.

Au - Gonzalez Malagon, S.G., Au - Dobson, L., Au - Muñoz, A.M.L., Au - Dawson, M., Au - Barrell, W., Au - Marangos, P., Au - Krause, M., and Au - Liu, K.J. (2019). Dissection, culture and analysis of primary cranial neural crest cells from mouse for the study of neural crest cell delamination and migration. JoVE, e60051.

Badri, K.R., Gao, L., Hyjek, E., Schuger, N., Schuger, L., Qin, W., Chekaluk, Y., Kwiatkowski, D.J., and Zhe, X. (2013). Exonic mutations of TSC2/TSC1 are common but not seen in all sporadic pulmonary lymphangioleiomyomatosis. Am. J. Respir. Crit. Care Med. *187*, 663–665.

Baggiolini, A., Varum, S., Mateos, J.M., Bettosini, D., John, N., Bonalli, M., Ziegler, U., Dimou, L., Clevers, H., Furrer, R., et al. (2015). Premigratory and migratory neural crest cells are multipotent in vivo. Cell Stem Cell *16*, 314–322.

Baroffio, A., Dupin, E., and Le Douarin, N.M. (1991). Common precursors for neural and mesectodermal derivatives in the cephalic neural crest. Development *112*, 301.

Barrera, P., Simons, S.O., Luijk, B., Wessels, M.J., and Heijdra, Y.F. (2013). Efficacy of sirolimus therapy for chylous effusions in lymphangioleiomyomatosis. Ann. Am. Thorac. Soc. *10*, 408–409.

Beauchamp, R.L., Banwell, A., McNamara, P., Jacobsen, M., Higgins, E., Northrup, H., Short, P., Sims, K., Ozelius, L., and Ramesh, V. (1998). Exon scanning of the entire TSC2 gene for germline mutations in 40 unrelated patients with tuberous sclerosis. Hum. Mutat. *12*, 408–416.

Bee, J., Fuller, S., Miller, S., and Johnson, S.R. (2018). Lung function response and side effects to rapamycin for lymphangioleiomyomatosis: a prospective national cohort study. Thorax *73*, 369–375.

Berner, J.M., Meza-Zepeda, L.A., Kools, P.F., Forus, A., Schoenmakers, E.F., Van de Ven, W.J., Fodstad, O., and Myklebost, O. (1997). HMGIC, the gene for an architectural transcription factor, is amplified and rearranged in a subset of human sarcomas. Oncogene *14*, 2935–2941.

Bhatt, S., Diaz, R., and Trainor, P.A. (2013). Signals and switches in Mammalian neural crest cell differentiation. Cold Spring Harb. Perspect. Biol. *5*, a008326.

Bissler, J.J., McCormack, F.X., Young, L.R., Elwing, J.M., Chuck, G., Leonard, J.M., Schmithorst, V.J., Laor, T., Brody, A.S., Bean, J., et al. (2008). Sirolimus for angiomyolipoma in tuberous sclerosis complex or lymphangioleiomyomatosis. N. Engl. J. Med. *358*, 140–151.

Brigo, F., Lattanzi, S., Trinka, E., Nardone, R., Bragazzi, N.L., Ruggieri, M., Martini, M., and Walusinski, O. (2018). First descriptions of tuberous sclerosis by Désiré-Magloire Bourneville (1840–1909). Neuropathology *38*, 577–582.

Calloni, G.W., Le Douarin, N.M., and Dupin, E. (2009). High frequency of cephalic neural crest cells shows coexistence of neurogenic, melanogenic, and osteogenic differentiation capacities. Proc. Natl. Acad. Sci. U S A *106*, 8947.

Carsillo, T., Astrinidis, A., and Henske, E.P. (2000). Mutations in the tuberous sclerosis complex gene TSC2 are a cause of sporadic pulmonary lymphangioleiomyomatosis. Proc. Natl. Acad. Sci. U S A *97*, 6085–6090.

Chiappetta, G., Avantaggiato, V., Visconti, R., Fedele, M., Battista, S., and Trapasso, F. (1996). High level expression of the HMGI (Y) gene during embryonic development. Oncogene *13*, 2439–2446.

Clements, D., Dongre, A., Krymskaya, V.P., and Johnson, S.R. (2015). Wild type mesenchymal cells contribute to the lung pathology of lymphangioleiomyomatosis. PLoS One *10*, e0126025.

Clements, D., Miller, S., and Johnson, S.R. (2020). Pulmonary Lymphangioleiomyomatosis originates in the pleural mesothelial cell population. Med. Hypotheses *141*, 109703.

D'Armiento, J., Imai, K., Schiltz, J., Kolesnekova, N., Sternberg, D., Benson, K., Pardo, A., Selman, M., Smolarek, T., Vundavalli, M., et al. (2007). Identification of the benign mesenchymal tumor gene HMGA2 in lymphangiomyomatosis. Cancer Res. *67*, 1902–1909.

D'Armiento, J., Shiomi, T., Marks, S., Geraghty, P., Sankarasharma, D., and Chada, K. (2016). Mesenchymal tumorigenesis driven by TSC2 haploinsufficiency requires HMGA2 and is independent of mTOR pathway activation. Cancer Res. *76*, 844–854.

Dabora, S.L., Jozwiak, S., Franz, D.N., Roberts, P.S., Nieto, A., Chung, J., Choy, Y.S., Reeve, M.P., Thiele, E., Egelhoff, J.C., et al. (2001). Mutational analysis in a cohort of 224 tuberous sclerosis patients indicates increased severity of TSC2, compared with TSC1, disease in multiple organs. Am. J. Hum. Genet. *68*, 64–80.

Davies, D.M., de Vries, P.J., Johnson, S.R., McCartney, D.L., Cox, J.A., Serra, A.L., Watson, P.C., Howe, C.J., Doyle, T., Pointon, K., et al. (2011). Sirolimus therapy for angiomyolipoma in tuberous sclerosis and sporadic lymphangioleiomyomatosis: a phase 2 trial. Clin. Cancer Res. *17*, 4071–4081.

de Vries, P.J., Whittemore, V.H., Leclezio, L., Byars, A.W., Dunn, D., Ess, K.C., Hook, D., King, B.H., Sahin, M., and Jansen, A. (2015). Tuberous sclerosis associated neuropsychiatric disorders (TAND) and the TAND Checklist. Pediatr. Neurol. *52*, 25–35.

Delaney, S.P., Julian, L.M., Pietrobon, A., Yockell-Lelièvre, J., Doré, C., Wang, T.T., Doyon, V.C., Raymond, A., Patten, D.A., Kristof, A.S., et al. (2020). Human pluripotent stem cell modeling of tuberous sclerosis complex reveals lineage-specific therapeutic vulnerabilities. bioRxiv, 683359.

Delaney, S.P., Julian, L.M., and Stanford, W.L. (2014). The neural crest lineage as a driver of disease heterogeneity in Tuberous Sclerosis Complex and Lymphangioleiomyomatosis. Front. Cell Dev. Biol. *2*, 69.

Dixon, B.P., Hulbert, J.C., and Bissler, J.J. (2011). Tuberous sclerosis complex renal disease. Nephron Exp. Nephrol. *118*, e15–e20.

Duband, J.L. (2000-2013). Neural crest delamination and migration: integrating regulations of cell interactions, locomotion, survival and fate. In Madame Curie Bioscience Database (Landes Bioscience), pp. 1–42.

Duband, J.L., Monier, F., Delannet, M., and Newgreen, D. (1995). Epithelium-mesenchyme transition during neural crest development. Acta Anat. (Basel) *154*, 63–78.

Dupin, E., and Coelho-Aguiar, J.M. (2013). Isolation and differentiation properties of neural crest stem cells. Cytometry. A *83*, 38–47.

El-Hashemite, N., Zhang, H., Henske, E.P., and Kwiatkowski, D.J. (2003). Mutation in TSC2 and activation of mammalian target of rapamycin signalling pathway in renal angiomyolipoma. Lancet *361*, 1348–1349.

Fang, F., Sun, S., Wang, L., Guan, J.L., Giovannini, M., Zhu, Y., and Liu, F. (2015). Neural crest-specific TSC1 deletion in mice leads to sclerotic craniofacial bone lesion. J. Bone Miner Res. *30*, 1195–1205.

Faustino-Rocha, A., Oliveira, P.A., Pinho-Oliveira, J., Teixeira-Guedes, C., Soares-Maia, R., da Costa, R.G., Colaço, B., Pires, M.J., Colaço, J., Ferreira, R., et al. (2013). Estimation of rat mammary tumor volume using caliper and ultrasonography measurements. Lab. Anim. *42*, 217–224.

Feliciano, D.M. (2020). The neurodevelopmental pathogenesis of tuberous sclerosis complex (TSC). Front. Neuroanat. *14*, 39.

Feliciano, D.M., Quon, J.L., Su, T., Taylor, M.M., and Bordey, A. (2012). Postnatal neurogenesis generates heterotopias, olfactory micronodules and cortical infiltration following single-cell Tsc1 deletion. Hum. Mol. Genet. *21*, 799–810.

Ferrans, V.J., Yu, Z.X., Nelson, W.K., Valencia, J.C., Tatsuguchi, A., Avila, N.A., Riemenschn, W., Matsui, K., Travis, W.D., and Moss, J. (2000). Lymphangioleiomyomatosis (LAM): a review of clinical and morphological features. J. Nippon Med. Sch. *67*, 311–329.

Festing, M.F. (2006). Design and statistical methods in studies using animal models of development. ILAR J. *47*, 5–14.

Festing, M.F., and Altman, D.G. (2002). Guidelines for the design and statistical analysis of experiments using laboratory animals. ILAR J. *43*, 244–258.

Franz, D.N., Belousova, E., Sparagana, S., Bebin, E.M., Frost, M., Kuperman, R., Witt, O., Kohrman, M.H., Flamini, J.R., Wu, J.Y., et al. (2013). Efficacy and safety of everolimus for subependymal giant cell astrocytomas associated with tuberous sclerosis complex (EXIST-1): a multicentre, randomised, placebo-controlled phase 3 trial. Lancet *381*, 125–132.

Giannikou, K., Malinowska, I.A., Pugh, T.J., Yan, R., Tseng, Y.Y., Oh, C., Kim, J., Tyburczy, M.E., Chekaluk, Y., Liu, Y., et al. (2016). Whole exome sequencing identifies TSC1/TSC2 biallelic loss as the primary and sufficient driver event for renal angiomyolipoma development. PLoS Genet. *12*, e1006242.

Goncharova, E.A., Goncharov, D.A., Eszterhas, A., Hunter, D.S., Glassberg, M.K., Yeung, R.S., Walker, C.L., Noonan, D., Kwiatkowski, D.J., Chou, M.M., et al. (2002). Tuberin regulates p70 S6 kinase activation and ribosomal protein S6 phosphorylation. A role for the TSC2 tumor suppressor gene in pulmonary lymphangioleiomyomatosis (LAM). J. Biol. Chem. *277*, 30958–30967.

Guo, M., Yu, J.J., Perl, A.K., Wikenheiser-Brokamp, K.A., Riccetti, M., Zhang, E.Y., Sudha, P., Adam, M., Potter, A., Kopras, E.J., et al. (2020). Single-cell transcriptomic analysis identifies a unique pulmonary lymphangioleiomyomatosis cell. Am. J. Respir. Crit. Care Med. *202*, 1373–1387.

Hagedorn, L., Suter, U., and Sommer, L. (1999). P0 and PMP22 mark a multipotent neural crest-derived cell type that displays community effects in response to TGF-beta family factors. Development *126*, 3781–3794.

Hartman, T.R., Liu, D., Zilfou, J.T., Robb, V., Morrison, T., Watnick, T., and Henske, E.P. (2009). The tuberous sclerosis proteins regulate formation of the primary cilium via a rapamycin-insensitive and polycystin 1-independent pathway. Hum. Mol. Genet. *18*, 151–163.

Henske, E.P., Jozwiak, S., Kingswood, J.C., Sampson, J.R., and Thiele, E.A. (2016). Tuberous sclerosis complex. Nat. Rev. Dis. Primers *2*, 16035.

Henske, E.P., and McCormack, F.X. (2012). Lymphangioleiomyomatosis - a wolf in sheep's clothing. J. Clin. Invest. *122*, 3807–3816.

Higa, F., Uchihara, T., Haranaga, S., Yara, S., Tateyama, M., Oshiro, Y., Shiraishi, M., Kumasaka, T., Seyama, K., and Fujita, J. (2009). Malignant epithelioid angiomyolipoma in the kidney and liver of a patient with pulmonary lymphangioleiomyomatosis: lack of response to sirolimus. Intern. Med. *48*, 1821–1825.

Hock, R., Witte, F., Brocher, J., Schutz, M., and Scheer, U. (2006). Expression of HMGA2 variants during oogenesis and early embryogenesis of Xenopus laevis. Eur. J. Cell Biol. *85*, 519–528.

Hunter, D.S., Klotzbucher, M., Kugoh, H., Cai, S.L., Mullen, J.P., Manfioletti, G., Fuhrman, U., and Walker, C.L. (2002). Aberrant expression of HMGA2 in uterine leiomyoma associated with loss of TSC2 tumor suppressor gene function. Cancer Res. *62*, 3766–3772.

Inoki, K., Li, Y., Xu, T., and Guan, K.L. (2003). Rheb GTPase is a direct target of TSC2 GAP activity and regulates mTOR signaling. Genes Dev. *17*, 1829–1834.

Johnson, S.R., Clelland, C.A., Ronan, J., Tattersfield, A.E., and Knox, A.J. (2002). The TSC-2 product tuberin is expressed in lymphangioleiomyomatosis and angiomyolipoma. Histopathology *40*, 458–463.

Jones, A.C., Shyamsundar, M.M., Thomas, M.W., Maynard, J., Idziaszczyk, S., Tomkins, S., Sampson, J.R., and Cheadle, J.P. (1999). Comprehensive mutation analysis of TSC1 and TSC2-and phenotypic correlations in 150 families with tuberous sclerosis. Am. J. Hum. Genet. *64*, 1305–1315.

Julian, L.M., Delaney, S.P., Wang, Y., Goldberg, A.A., Doré, C., Yockell-Lelièvre, J., Tam, R.Y., Giannikou, K., McMurray, F., Shoichet, M.S., et al. (2017). Human pluripotent stem cell-derived TSC2-haploinsufficient smooth muscle cells recapitulate features of lymphangioleiomyomatosis. Cancer Res. *77*, 5491–5502.

Kaku, M., Komatsu, Y., Mochida, Y., Yamauchi, M., Mishina, Y., and Ko, C.-C. (2012). Identification and characterization of neural crest-derived cells in adult periodontal ligament of mice. Arch. Oral Biol. *57*, 1668–1675.

Kazmierczak, B., Rosigkeit, J., Wanschura, S., Meyer-Bolte, K., Van de Ven, W.J., Kayser, K., Krieghoff, B., Kastendiek, H., Bartnitzke, S., and Bullerdiek, J. (1996). HMGI-C rearrangements as the molecular basis for the majority of pulmonary chondroid hamartomas: a survey of 30 tumors. Oncogene *12*, 515–521.

Kenerson, H., Folpe, A.L., Takayama, T.K., and Yeung, R.S. (2007). Activation of the mTOR pathway in sporadic angiomyolipomas and other perivascular epithelioid cell neoplasms. Hum. Pathol. *38*, 1361–1371.

Kingswood, C., Bolton, P., Crawford, P., Harland, C., Johnson, S.R., Sampson, J.R., Shepherd, C., Spink, J., Demuth, D., Lucchese, L., et al. (2016). The clinical profile of tuberous sclerosis complex (TSC) in the United Kingdom: a retrospective cohort study in the Clinical Practice Research Datalink (CPRD). Eur. J. Paediatr. Neurol. *20*, 296–308.

Kobayashi, T., Minowa, O., Kuno, J., Mitani, H., Hino, O., and Noda, T. (1999). Renal carcinogenesis, hepatic hemangiomatosis, and embryonic lethality caused by a germ-line Tsc2 mutation in mice. Cancer Res. *59*, 1206–1211.

Krispin, S., Nitzan, E., Kassem, Y., and Kalcheim, C. (2010). Evidence for a dynamic spatiotemporal fate map and early fate restrictions of premigratory avian neural crest. Development *137*, 585.

Kwiatkowski, D.J. (2010). Animal models of lymphangioleiomyomatosis (LAM) and tuberous sclerosis complex (TSC). Lymphat Res. Biol. *8*, 51–57.

Lam, H.C., Siroky, B.J., and Henske, E.P. (2018). Renal disease in tuberous sclerosis complex: pathogenesis and therapy. Nat. Rev. Nephrol. *14*, 704–716.

Lee, P.S., Tsang, S.W., Moses, M.A., Trayes-Gibson, Z., Hsiao, L.L., Jensen, R., Squillace, R., and Kwiatkowski, D.J. (2010). Rapamycin-insensitive up-regulation of MMP2 and other genes in tuberous sclerosis complex 2-deficient lymphangioleiomyomatosis-like cells. Am. J. Respir. Cell Mol. Biol. *42*, 227–234.

Li, C., Zhang, E., Sun, Y., Lee, P.S., Zhan, Y., Guo, Y., Osorio, J.C., Rosas, I.O., Xu, K.F., Kwiatkowski, D.J., et al. (2014). Rapamycin-insensitive up-regulation of adipocyte phospholipase A2 in tuberous sclerosis and lymphangioleiomyomatosis. PLoS One *9*, e104809.

Lin, T.V., Hsieh, L., Kimura, T., Malone, T.J., and Bordey, A. (2016). Normalizing translation through 4E-BP prevents mTOR-driven cortical mislamination and ameliorates aberrant neuron integration. Proc. Natl. Acad. Sci. U S A *113*, 11330.

Liu, Z., Jin, Y.Q., Chen, L., Wang, Y., Yang, X., Cheng, J., Wu, W., Qi, Z., and Shen, Z. (2015). Specific marker expression and cell state of Schwann cells during culture in vitro. PLoS One *10*, e0123278.

Macri, S., Simula, L., Pellarin, I., Pegoraro, S., Onorati, M., Sgarra, R., Manfioletti, G., and Vignali, R. (2016). Hmga2 is required for neural crest cell specification in Xenopus laevis. Dev. Biol. *411*, 25–37.

Maguire, L.H., Thomas, A.R., and Goldstein, A.M. (2015). Tumors of the neural crest: common themes in development and cancer. Dev. Dyn. *244*, 311–322.

Martin, K.R., Zhou, W., Bowman, M.J., Shih, J., Au, K.S., Dittenhafer-Reed, K.E., Sisson, K.A., Koeman, J., Weisenberger, D.J., Cottingham, S.L., et al. (2017). The genomic landscape of tuberous sclerosis complex. Nat. Commun. *8*, 15816.

McCormack, F.X., Inoue, Y., Moss, J., Singer, L.G., Strange, C., Nakata, K., Barker, A.F., Chapman, J.T., Brantly, M.L., Stocks, J.M., et al. (2011). Efficacy and safety of sirolimus in lymphangioleiomyomatosis. New Engl. J. Med. *364*, 1595–1606.

Minarcik, J.C., and Golden, J.A. (2003). AP-2 and HNK-1 define distinct populations of cranial neural crest cells. Orthod. Craniofac. Res. *6*, 210–219.

Motohashi, T., Yamanaka, K., Chiba, K., Miyajima, K., Aoki, H., Hirobe, T., and Kunisada, T. (2011). Neural crest cells retain their capability for multipotential differentiation even after lineage-restricted stages. Dev. Dyn. *240*, 1681–1693.

Neelisetty, S., Alford, C., Reynolds, K., Woodbury, L., Nlandu-Khodo, S., Yang, H., Fogo, A.B., Hao, C.M., Harris, R.C., Zent, R., et al. (2015). Renal fibrosis is not reduced by blocking transforming growth factor-β signaling in matrix-producing interstitial cells. Kidney Int. *88*, 503–514.

Niida, Y., Lawrence-Smith, N., Banwell, A., Hammer, E., Lewis, J., Beauchamp, R.L., Sims, K., Ramesh, V., and Ozelius, L. (1999). Analysis of both TSC1 and TSC2 for germline mutations in 126 unrelated patients with tuberous sclerosis. Hum. Mutat. *14*, 412–422.

Niida, Y., Stemmer-Rachamimov, A.O., Logrip, M., Tapon, D., Perez, R., Kwiatkowski, D.J., Sims, K., MacCollin, M., Louis, D.N., and Ramesh, V. (2001). Survey of somatic mutations in tuberous sclerosis complex (TSC) hamartomas suggests different genetic mechanisms for pathogenesis of TSC lesions. Am. J. Hum. Genet. *69*, 493–503.

Nishino, J., Kim, I., Chada, K., and Morrison, S.J. (2008). Hmga2 promotes neural stem cell self-renewal in young but not old mice by reducing

p16Ink4a and p19Arf Expression. Cell *135*, 227–239.

Onda, H., Lueck, A., Marks, P.W., Warren, H.B., and Kwiatkowski, D.J. (1999). Tsc2(+/–) mice develop tumors in multiple sites that express gelsolin and are influenced by genetic background. J. Clin. Invest. *104*, 687–695.

Osumi-Yamashita, N., Ninomiya, Y., Doi, H., and Eto, K. (1994). The contribution of both forebrain and midbrain crest cells to the mesenchyme in the frontonasal mass of mouse embryos. Dev. Biol. *164*, 409–419.

Pacheco-Rodriguez, G., and Moss, J. (2010). The role of chemokines in migration of metastatic-like lymphangioleiomyomatosis cells. Crit. Rev. Immunol. *30*, 387–394.

Park, S.M., Lim, J.S., Ramakrishina, S., Kim, S.H., Kim, W.K., Lee, J., Kang, H.C., Reiter, J.F., Kim, D.S., Kim, H.H., et al. (2018). Brain somatic mutations in MTOR disrupt neuronal ciliogenesis, leading to focal cortical dyslamination. Neuron *99*, 83–97.e7.

Peri, S., Caretti, E., Tricarico, R., Devarajan, K., Cheung, M., Sementino, E., Menges, C.W., Nicolas, E., Vanderveer, L.A., Howard, S., et al. (2017). Haploinsufficiency in tumor predisposition syndromes: altered genomic transcription in morphologically normal cells heterozygous for VHL or TSC mutation. Oncotarget *8*, 17628–17642.

Pfaltzgraff, E.R., Mundell, N.A., and Labosky, P.A. (2012). Isolation and culture of neural crest cells from embryonic murine neural tube. J. Vis. Exp. e4134.

Qin, W., Bajaj, V., Malinowska, I., Lu, X., MacConaill, L., Wu, C.L., and Kwiatkowski, D.J. (2011). Angiomyolipoma have common mutations in TSC2 but no other common genetic events. PLoS One *6*, e24919.

Rakowski, S.K., Winterkorn, E.B., Paul, E., Steele, D.J., Halpern, E.F., and Thiele, E.A. (2006). Renal manifestations of tuberous sclerosis complex: incidence, prognosis, and predictive factors. Kidney Int. *70*, 1777–1782.

Ren, S., Luo, Y., Chen, H., Warburton, D., Lam, H.C., Wang, L.L., Chen, P., Henske, E.P., and Shi, W. (2016). Inactivation of Tsc2 in mesoderm-derived cells causes polycystic kidney lesions and impairs lung alveolarization. Am. J. Pathol. *186*, 3261–3272.

Sancak, O., Nellist, M., Goedbloed, M., Elfferich, P., Wouters, C., Maat-Kievit, A., Zonnenberg, B., Verhoef, S., Halley, D., and van den Ouweland, A. (2005). Mutational analysis of the TSC1 and TSC2 genes in a diagnostic setting: genotype–phenotype correlations and comparison of diagnostic DNA techniques in Tuberous Sclerosis Complex. Eur. J. Hum. Genet. *13*, 731–741.

Sápi, J., Kovács, L., Drexler, D.A., Kocsis, P., Gajári, D., and Sápi, Z. (2015). Tumor volume estimation and quasi-continuous administration for most effective bevacizumab therapy. PLoS One *10*, e0142190.

Sato, T., Seyama, K., Fujii, H., Maruyama, H., Setoguchi, Y., Iwakami, S., Fukuchi, Y., and Hino, O. (2002). Mutation analysis of the TSC1 and TSC2 genes in Japanese patients with pulmonary lymphangioleiomyomatosis. J. Hum. Genet. *47*, 20–28.

Serbedzija, G.N., Bronner-Fraser, M., and Fraser, S.E. (1992). Vital dye analysis of cranial neural crest cell migration in the mouse embryo. Development *116*, 297.

Siroky, B.J., Yin, H., and Bissler, J.J. (2011). Clinical and molecular insights into tuberous sclerosis complex renal disease. Pediatr. Nephrol. *26*, 839–852.

Smolarek, T.A., Wessner, L.L., McCormack, F.X., Mylet, J.C., Menon, A.G., and Henske, E.P. (1998). Evidence that lymphangiomyomatosis is caused by TSC2 mutations: chromosome 16p13 loss of heterozygosity in angiomyolipomas and lymph nodes from women with lymphangiomyomatosis. Am. J. Hum. Genet. *62*, 810–815.

Sowa, Y., Imura, T., Numajiri, T., Takeda, K., Mabuchi, Y., Matsuzaki, Y., and Nishino, K. (2013). Adipose stromal cells contain phenotypically distinct adipogenic progenitors derived from neural crest. PLoS One *8*, e84206.

Tallini, G., Vanni, R., Manfioletti, G., Kazmierczak, B., Faa, G., Pauwels, P., Bullerdiek, J., Giancotti, V., Van Den Berghe, H., and Dal Cin, P. (2000). HMGI-C and HMGI(Y) immunoreactivity correlates with cytogenetic abnormalities in lipomas, pulmonary chondroid hamartomas, endometrial polyps, and uterine leiomyomas and is compatible with rearrangement of the HMGI-C and HMGI(Y) genes. Lab. Invest. *80*, 359–369.

Tam, R.Y., Yockell-Lelièvre, J., Smith, L.J., Julian, L.M., Baker, A.E.G., Choey, C., Hasim, M.S., Dimitroulakos, J., Stanford, W.L., and Shoichet, M.S. (2019). Rationally designed 3D hydrogels model invasive lung diseases enabling high-content drug screening. Adv. Mater. *31*, e1806214.

Taveira-DaSilva, A.M., and Moss, J. (2015). Clinical features, epidemiology, and therapy of lymphangioleiomyomatosis. Clin. Epidemiol. *7*, 249–257.

Tyburczy, M.E., Dies, K.A., Glass, J., Camposano, S., Chekaluk, Y., Thorner, A.R., Lin, L., Krueger, D., Franz, D.N., Thiele, E.A., et al. (2015). Mosaic and intronic mutations in TSC1/TSC2 explain the majority of TSC patients with No mutation identified by conventional testing. PLoS Genet. *11*, e1005637.

Van Sluyters, R.C., Ballinger, B., Bayne, K., Cunningham, C., Degryse, A.-D., Dubner, R., Evans, H., Gdowski, M.J., Knight, R., Mench, J., et al. (2003). Guidelines for the Care and Use of Mammals in Neuroscience and Behavioral Research (National Academies Press (US)).

Wuidart, A., Ousset, M., Rulands, S., Simons, B.D., Van Keymeulen, A., and Blanpain, C. (2016). Quantitative lineage tracing strategies to resolve multipotency in tissue-specific stem cells. Genes Dev. *30*, 1261–1277.

Yamauchi, Y., Abe, K., Mantani, A., Hitoshi, Y., Suzuki, M., Osuzu, F., Kuratani, S., and Yamamura, K. (1999). A novel transgenic technique that allows specific marking of the neural crest cell lineage in mice. Dev. Biol. *212*, 191–203.

Yao, J., Taveira-DaSilva, A.M., Jones, A.M., Julien-Williams, P., Stylianou, M., and Moss, J. (2014). Sustained effects of sirolimus on lung function and cystic lung lesions in lymphangioleiomyomatosis. Am. J. Respir. Crit. Care Med. *190*, 1273–1282.

Yu, J., and Henske, E.P. (2010). mTOR activation, lymphangiogenesis, and estrogen-mediated cell survival: the "perfect storm" of pro-metastatic factors in LAM pathogenesis. Lymphat Res. Biol. *8*, 43–49.

Yu, J.J., Robb, V.A., Morrison, T.A., Ariazi, E.A., Karbowniczek, M., Astrinidis, A., Wang, C., Hernandez-Cuebas, L., Seeholzer, L.F., Nicolas, E., et al. (2009). Estrogen promotes the survival and pulmonary metastasis of tuberin-null cells. Proc. Natl. Acad. Sci. U S A *106*, 2635–2640.

STAR★METHODS

KEY RESOURCES TABLE

REAGENT or RESOURCE	SOURCE	IDENTIFIER
Antibodies		
Mouse monoclonal anti-CD57	Santa Cruz Biotechnology	Cat# sc-6261; RRID: AB_627130
Donkey anti-mouse IgG Alexa Fluor 488	Thermo Fisher Scientific	Cat# A21202; RRID:AB_141607
Chemicals, Peptides, and Recombinant Proteins		
DMEM/F12 (1:1)	Thermo Fisher Scientific	Cat# 11320033
EmbryoMax DMEM - High Glucose, Low Bicarbonate without sodium pyruvate	Millipore Sigma	Cat# SLM-220-M
ESGRO Leukemia Inhibitory Factor (LIF)	Millipore Sigma	Cat# ESG1106
Fetal bovine serum (FBS)	GE Healthcare Biosciences	Cat# SH30071.03
EmbryoMax ES Fetal Bovine Serum	Millipore Sigma	Cat# ES-009-C
Penicillin-Streptomycin	Thermo Fisher Scientific	Cat#15140122
Collagenase I	Worthington Biochemicals	Cat# LS004196
DNase I	Millipore Sigma	Cat# 4716728001
Elastase	Worthington Biochemicals	Cat# LS002294
Normal Donkey Serum	Sigma-Aldrich	Cat# D9663
Sodium Azide	Sigma-Aldrich	Cat# S2002
DRAQ5	Biolegend	Cat# 424101
Isoflurane	Henry Schein	Cat# 1311758
RBC Lysis Buffer	Santa Cruz Biotechnology	Cat# sc-296258
Sytox Green Nucleic Acid Stain	Thermo fisher Scientific	Cat# S7020
DAPI	Thermofisher Scientific	Cat# D1306
β-mercaptoethanol	Thermofisher Scientific	Cat# O3446I
Sodium Pyruvate	Thermofisher Scientific	Cat# 11-360-070
L-Glutamine	Millipore Sigma	Cat# G7513
Minimum essential media nonessential amino acids (MEM NEAA)	Thermofisher Scientific	Cat# 11095080
Basic fibroblast growth factor (bFGF)	Millipore Sigma	Cat# GF003
Triton X-100	Thermofisher Scientific	Cat# BP151-500
Bovine Serum Albumin	Millipore Sigma	Cat# A8412
Normal Donkey Serum	Millipore Sigma	Cat# D9663
Prolong Diamond Anti-fade Mountant with DAPI	Thermofisher Scientific	Cat#P36971
Critical Commercial Assays		
RNeasy Mini Kit	Qiagen Inc.	Cat# 74106
High-Capacity cDNA Reverse Transcription Kit	Thermo Fisher Scientific	Cat# 4368813
QIAamp DNA Mini Kit	Qiagen Inc.	Cat# 51304
Deposited data		
Original data for Figures 2J–2S	Mendeley	https://doi.org/10.17632/tsjk7wm5s8.1#file-7f9e656d-e11b-4ab4-be87-6e99139b3ab9
Experimental Models: Cell Lines		
STO Feeder Cell Line	ATCC	Cat# CRL:1503 **RRID:CVCL_3420**

(*Continued on next page*)

Continued

REAGENT or RESOURCE	SOURCE	IDENTIFIER
Experimental Models: Organisms/Strains		
Mus musculus: B6.Cg-Gt(ROSA)26Sor$^{tm9(CAG-tdTomato)Hze}$/J	The Jackson Laboratory	Cat# JAX:007909 **RRID:IMSR_JAX:007909**
Mus musculus: B6N.FVB-Tg(Mpz-Cre)26Mes/J	The Jackson Laboratory	Cat# JAX:017927 **RRID:IMSR_JAX:017927**
Mus musculus: B6. Cg-Mpz(Cre)$^{tm1.1JDar}$	This paper	N/A
Mus musculus: B6.129S4-Tsc2^{tm1Djk}/J Mus musculus	The Jackson Laboratory	Cat# JAX:004686 **RRID:IMSR_JAX:004686**
Mus musculus: C57Bl/6J	The Jackson Laboratory	Cat# JAX:000664 **RRID:IMSR_JAX:000664**
Oligonucleotides		
Primer: *R26R* - Forward	AAAGTCGCTCTGAGTTGTTAT	N/A
Primer: *R26R* - Reverse	GGAGCGGGAGAAATGGATATG	N/A
Primer: *Mpz* - Forward	CCACCACCTCTCCATTGCAC	N/A
Primer: *Mpz* – Reverse	ATGTTTAGCTGGCCCAAATG	N/A
Primer: *Tsc2* - Forward	CAAACCCACCTCCTCAAGCTTC	N/A
Primer: *Tsc2* – Reverse	AGACTGCCTTGGGAAAAGCG	N/A
Tsc2 (Mm00442004_m1)	Thermofisher Scientific	Cat# 4331182
CD57 (B3gat1) (Mm00661498_m1)	Thermofisher Scientific	Cat# 4331182
Tfap2aα (Mm00495574_m1)	Thermofisher Scientific	Cat# 4331182
Ngfr (Mm00446296_m1)	Thermofisher Scientific	Cat# 4331182
Sox10 (Mm00569909)	Thermofisher Scientific	Cat# 4331182
Software and Algorithms		
Prism 9 (version 9.11)	GraphPad Software	https://www.graphpad.com/scientific-software/prism/
VEVOLab 4.1	Visualsonics	https://www.visualsonics.com/product/software/vevo-lab
Paravision 6.0	Bruker	https://www.bruker.com/service/support-upgrades/software-downloads/mri.html
Living Image version 4.5	Perkin Elmer	https://www.perkinelmer.com/product/li-software-for-spectrum-1-seat-add-on-128113
GeneAmp 7900 SDS software	Thermofisher Scientific	https://www.thermofisher.com/order/catalog/product/4350490#/4350490

RESOURCE AVAILABILITY

Lead contact

Further information and requests for resources and reagents should be directed to and will be fulfilled by the Lead Contact, Jeanine D'Armiento (jmd12@cumc.columbia.edu).

Materials availability

This study did not generate new unique reagents.

Data and code availability

Original data for Figures 3A–3J in the paper is available (Mendeley Data DOI: https://doi.org/10.17632/tsjk7wm5s8.1#file-7f9e656d-e11b-4ab4-be87-6e99139b3ab9)

EXPERIMENTAL MODEL AND SUBJECT DETAILS

Mouse genetic studies

Animal experimentation was performed according to the Declaration of Helsinki convention for the use and care of animals and approved by the Institutional Animal Care and Use Committee (IACUC) at Columbia University Medical Center under protocol #AC-AAAR3401. The tuberous sclerosis *Tsc2*$^{+/-}$ transgenic

reporter mice was generated by crossing floxed B6.Cg-Gt(ROSA)26Sor$^{tm9(CAG-tdTomato)Hze}$/J reporter mice (JAX #007909, RRID:IMSR_JAX:007909) (female, N = 10 animals, 10 weeks old) with transgenic B6N.FVB-Tg(Mpz-Cre)26Mes/J mice (JAX #017927, RRID:IMSR_JAX:017927) (male, N = 10 animals; 10 weeks old) encoding a cell adhesion molecule myelin protein zero (P_0) promoter driving expression of cre recombinase specifically in neural crest and Schwann cells (Kaku et al., 2012; Sowa et al., 2013; Yamauchi et al., 1999). These mice were obtained from The Jackson Laboratory (Bar Harbor, ME) and maintained on a C57BL/6J background. B6. Cg-*Mpz(Cre)*$^{tm1.1JDar}$ progeny (male/female, N = 8 animals), obtained after backcrosses (N > 5) to *R26* mice, were then bred with tuberous sclerosis *Tsc2*$^{+/-}$ mice (RRID:IMSR_JAX:004686) (male/female, 10 weeks old, N = 10 animals) containing a neo-cassette targeted disruption of the second coding exon in the *Tsc2* gene (Onda et al., 1999). Following F1 hybrid crosses of *Tsc2*$^{+/-}$/*Mpz(Cre)*/TdT$^{fl/+}$ mice and genotyping analysis, *Tsc2*$^{+/-}$/*Mpz(Cre)*/TdT$^{fl/fl}$ (male/female, N = 22 animals), *Tsc2*$^{+/-}$/*Mpz(Cre)*/TdT$^{+/+}$ (male/female, N = 13 animals), *Tsc2*$^{+/+}$/*Mpz(Cre)*/TdT$^{fl/fl}$ (male/female, N = 15 animals), and control *Tsc2*$^{+/+}$/*Mpz(Cre)*/TdT$^{+/+}$ (male/female, N = 12 animals) mice development was monitored for 16 months and sacrificed for experiments. A schematic of genetic crosses involved in the development of this mouse model is displayed in Figure 1A. Tracking of spontaneous renal tumor development in all mouse genotypes commenced at 2 months of age, using tumor tracking protocols described below.

All mouse genotypes were confirmed by Southern hybridization of genomic DNA prepared from tail biopsies. Mouse sample sizes for each genotype utilized in this study are adequate to measure *Tsc2*$^{+/-}$-induced tumorigenesis detectable by tdTomato expression of neural crest cells expressing the Cre recombinase under the control of *Mpz* promoter, in comparison to mouse progeny wildtype for *Tsc2* and non-transgenic R26R mice. Given the time required for tumors to develop in the *Tsc2*$^{+/-}$ mice, the 80-90% rate of spontaneous tumorigenesis in the kidneys and liver, the number of pups per litter (~7 pups), the number of pups per litter yield for each genotype, the isogenicity of strains specified for genetic crosses, and comparative studies between mouse genotypes, such an assumption can be made for the four genotypes being compared, using mouse attrition rate of 8%, statistical power of 0.8 with double-sided α error of 0.05 (Festing and Altman, 2002). Blinding was assured in this study because mouse genetic crosses to obtain desired genotypes, assessments of resulting phenotypes, and selection of mice for comparative imaging studies, were all performed by an independent laboratory technician without knowledge of the hypothesis being tested. Genotyping results determined assignments of mouse pups to the different genetic backgrounds. Inbred littermates were used in each mouse genotype category and mice were age- and sex-matched for each group. Mouse littermates were also selected for genetic crosses at random. All attempts at replication in this study yielded successful reproducibility 90% of the time. All tumor tracking, measurement and excision experiments were repeated 2-3 times on different days per age group.

METHOD DETAILS

Tumor tracking protocols

Non-invasive monitoring of renal tumor development in the TS reporter mouse was performed by sequential IVIS spectral imaging, small animal ultrasound and confirmatory magnetic resonance imaging (MRI) as described below. Tumor monitoring began at 2 months of age with biweekly intervals up to 16 months of age. All animal imaging, data acquisition and analysis was performed at the Oncology and Precision Therapeutics and Imaging Core (OPTIC) of the Columbia University Medical Center in accordance with the guidance of the Institutional Animal Care and Use Committee.

Biofluorescence imaging. Mice were anesthetized with inhaled 2.5% isoflurane (Cat# 1311758, IsoThesia™, Henry Schein, Melville, NY), and the abdomen of the animal was fully shaved using electric shears and depilatory cream (Nair™ Church & Dwight Co. Trenton, NJ). Mice were then positioned supine on the warming stage of the In Vivo Imaging System (IVIS) Spectrum (Perkin Elmer, Santa Clara, CA) directly facing the camera sensor to monitor heart rate and body temperature, and capture fluorescence images. *In vivo* imaging system parameters were determined using standard optimization protocols with spectral unmixing. Each IVIS imaging procedure was completed within 5-10 minutes; animals were monitored until fully recovered from anesthesia. Fluorescence images were analyzed and total radiant efficiency ([photons/s]/[μW/cm^2]) calculated using the Living Image version 4.5 software (Perkin Elmer, Santa Clara, CA).

High frequency ultrasound imaging. Animals were anesthetized with 2.5% isoflurane (IsoThesia™, Henry Schein, Melville, NY) and placed on an electric heating pad to prevent hypothermia; abdominal hair was removed as described. Animals were positioned supine to monitor heart rate and body temperature.

Images of renal sagittal sections were obtained using the VisualSonics Vevo® 2100 Imaging System with 550D scan head (FUJIFILM VisualSonics Inc., Toronto, ON) at 55 megahertz. The 3-D Mode was used for advanced data acquisition and analysis, with virtual sections obtained in all directions (x-, y-, z- and other plane variations). Each ultrasound was completed within 10–15 minutes; animals were monitored until fully recovered from anesthesia. Ultrasound images were analyzed using the VEVOLab 4.1 software provided by Visualsonics (Toronto, ON).

Magnetic Resonance Imaging (MRI). The MRI examination of the abdomen of the mice was performed to confirm findings of ultrasound scans in some experimental mice. MRI was performed with a 9.4 Tesla animal scanner (Bruker BioSpin, Germany). Animals were anesthetized by inhalation of isoflurane (IsoThesia™, Henry Schein, Melville, NY) (3% induction and 1-2% maintenance) and were kept homeothermic by a water-circulating system to keep the MRI bed at 37°C. A Rapid Imaging with Refocused Echoes sequence was used to acquire multi-slice images in the long axis of both kidneys by using the following parameters: TR/TE = 2600/30 ms, averages = 4, RARE factor = 8, matrix = 256x256, field of view = 40x40 mm^2, slice thickness = 0.5 mm. MRI images were analyzed utilizing the Paravision 6.0 software from Bruker BioSpin.

Mouse renal tumor processing and flow cytometry

Individual renal tumor length and width per kidney pair per mice were measured using digital calipers following mice sacrifice. Tumor volumes were estimated using the formular: ($Width^2$ X Length)/2 (Faustino-Rocha et al., 2013; Sápi et al., 2015). Renal tumor and tissues biopsied from $Tsc2^{+/-}$/*Mpz(Cre)*/$TdT^{fl/fl}$, $Tsc2^{+/-}$/*Mpz(Cre)*/$TdT^{+/+}$, $Tsc2^{+/+}$/*Mpz(Cre)* /$TdT^{fl/fl}$, and control $Tsc2^{+/+}$/*Mpz(Cre)*/$TdT^{+/+}$ mice at 4, 6, 12, and 16 months were pooled by age group and digested into single cell suspension (Neelisetty et al., 2015). Samples were minced in DMEM-F12 media supplemented with 2% fetal bovine serum (FBS) (#SH30071.03, Hyclone, GE Healthcare Biosciences, Piscataway, NJ) using fine sterile razors and digested with a cocktail of collagenase I (170mg/L, Cat# LS004196, Worthington Biochemical, Lakewood, NJ), DNase I (0.33 U/ml; Cat# 4716728001, Millipore Sigma, St. Louis, MO) and elastase (0.075 U/ml, Cat# LS002294, Worthington Biochemical, Lakewood, NJ) in a shaker at a speed of 85rpm at 37°C for 45 mins. Tissue particles were vigorously triturated and re-incubated in the same conditions for another 30 mins then passed through 100μm, 70μm, and 40μm cell strainers sequentially. Cell suspensions were centrifuged for 5 min at 300 x g at room temperature, supernatant aspirated, and the erythrocytes lysed using 1× RBC lysis buffer (Cat# sc-296258, Santa Cruz Biotechnology, Dallas, TX) for 10 mins. Following subsequent centrifugation for 5 min at 300 x g, cell pellets were resuspended in PBS containing 2% FBS and DAPI (Cat# D1306, Thermofisher Scientific, Grand Island, NY) or Sytox green viability dye (Cat# S7020, Thermofisher Scientific, Grand Island, NY) in the dark for 10 mins. Cells were washed in cold PBS, filtered with 40μm cell strainer, and resuspended in PBS containing 2% FBS, DNase I for cell sorting, and DRAQ5 (1:1000, Cat# 424101, BioLegend, San Diego, CA) in some experiments to distinguish viable cells. Flow cytometry was performed using a BD FACS Aria II (Becton Dickinson, Franklin Lakes, NJ, USA) at the Columbia Stem Cell Initiative (CSCI) Flow Cytometry Core Facility and cells were sorted into tubes pre-incubated with DMEM-F12 containing 2% FBS. Single cells were sequentially selected on FSC-A/SSC-A and FSC-A/FSC-H dot plots and band-pass filters 586/15, 530/30, 450/50, or 715/50 were used to acquire tdTomato and viability dye signals. Tubes with unstained cells were used to set compensation and at least 50,000 events were collected for each tumor or tissue sample sorted into $tdTomato^{(+)}$ vs $tdTomato^{(-)}$ fractions per experiment. Data analysis was performed using FlowJo 10.7.1 (BD Biosciences, Franklin Lakes, NJ) or FCS Express 7 Plus (De Novo Software, Glendale, CA).

Neural crest cell culture

Cranial (CNCC) and trunk (TNCC) neural crest cells were used as positive comparative controls for flow cytometry and RT-qPCR experiments. These tissues were obtained from 9.5dpc $Tsc2^{+/-}$/*Mpz(Cre)*/$TdT^{fl/fl}$ fetal mice excavated from pregnant dam. Isolation of CNCCs was performed by cutting a region between head fold and the anterior tip of the otic placode of mouse embryos (Au - Gonzalez Malagon et al., 2019) under a dissecting microscope, while TNCCs were obtained by excising embryonic neural tube between somites 16-22 (Pfaltzgraff et al., 2012). Tissue dissects were placed in the center of sterile matrigel-coated petri dishes containing neural crest media and incubated at 37°C in 5% CO_2 to allow for migration of NCCs away from the neural tube. NCC media was conditioned using STO feeder cells (mouse embryonic fibroblasts) (ATCC Cat# CRL-1503, RRID:CVCL_3420) grown overnight in Dulbecco's modified Eagle's medium (DMEM, 4500mg/L glucose) (Cat# SLM-220-M, Millipore Sigma, St. Louis, MO) containing 15% fetal bovine serum (FBS) (Cat# ES-009-C, Millipore Sigma, St. Louis, MO), 0.1mM minimum essential media nonessential amino acids (MEM NEAA 100X) (Cat# 11095080), 1 mM sodium pyruvate (Cat# 11-360-070, Thermofisher

Scientific, Grand Island, NY), 55 μM β-mercaptoethanol (Cat# O3446I-100, Thermofisher Scientific, Grand Island, NY), 100 units/mL penicillin-streptomycin (Cat#15140122, Thermofisher Scientific, Grand Island, NY) and 2 mM L-glutamine (Cat# G7513, Millipore Sigma, St. Louis, MO). Conditioned media was thereafter supplemented with basic fibroblast growth factor (bFGF, 25ng/ml) (Cat# GF003, Millipore Sigma, St. Louis, MO) and leukemia inhibition factor (LIF, 1000U) (Cat# ESG1106, Millipore Sigma, St. Louis, MO). 48hrs after NCC migration from neural tube, explant tissue is removed and NCCs routinely passaged. NCCs were incubated in DAPI viability dyes for 10 mins prior to flow cytometry experiments.

Immunohistochemistry. Renal tumor and tissues of differentially aged mice were excised, briefly washed in PBS and immediately fixed in 4% paraformaldehyde (PFA) for 2 hours at room temperature. Renal tumors and tissues are then rinsed in PBS and incubated overnight at 4°C in 30% sucrose to preserve endogenous protein expression (Wuidart et al., 2016). Thereafter, fixed tissues/tumors were immediately embedded in OCT compound, snap-frozen in isopentane mixed with dry ice and kept at -80°C. Embedded tissues were used to obtain 4 μM thick sections at the Molecular Pathology Core Facility at Columbia University Medical Center.

For *CD57* (β-1,3-glucuronyltransferase (B3GAT1)) immunolabeling (sc-6261; RRID: AB_627130; Santa Cruz Biotechnologies, Dallas, TX), tissue/tumor slices were blocked and permeabilized for 1 hour at room temperature using a mixture of 0.3% Triton X-100 (Cat# BP151-500, Thermofisher Scientific, Grand Island, NY), 1% bovine serum albumin (BSA) (Cat# 8412, Millipore Sigma, St. Louis, MO) and 10% normal donkey serum (NDS) (Cat# D9663, Millipore Sigma, St. Louis, MO), and incubated overnight at 4°C in anti-CD57 diluted in antibody dilution buffer (1% BSA, 1% NDS, 0.3% Triton X-100, 0.01% sodium azide). Following 1-hr secondary antibody incubation using donkey anti-mouse Alexa Fluor 488 (Cat# A21202, RRID:AB_141607, Thermofisher Scientific, Grand Island, NY), slides were cover-slipped using Prolong Diamond Anti-fade Mountant with DAPI (Cat# P36971, Thermofisher Scientific, Grand Island, NY) and visualized using Ti-E Eclipse inverted fluorescent or confocal microscope (Nikon Instruments Inc., Melville, NY). Immunohistochemistry experiments were repeated twice for each aged mice timepoint using N=3 slides per tissue/tumor, 2-3 sections per slide. The use of mouse tissue samples was approved by the IACUC protocol #AC-AAAR3401.

RT-qPCR and southern blot. Total RNA was isolated from mouse renal tumors and tissue biopsies excised from all mouse genotypes. RNA isolation was performed using RNeasy Mini Kit (#74106, Qiagen Inc., Valencia, CA). High-quality RNA was ensured by UV spectroscopy and incorporating DNase treatment in the protocol. Reverse transcription was performed using the High-Capacity cDNA Reverse Transcription Kit (#4368813; Applied Biosystems, Thermofisher Scientific, Grand Island, NY, USA) (Qin et al., 2011). Quantification of gene expression was assessed in quadruplicates per biological replicate by reverse transcription qPCR using TaqMan probes with FAM dye labels (Thermofisher Scientific, Grand Island, NY), mouse primers for *Tsc2* (Mm00442004_m1), *B3gat1* (Mm00661498_m1), *Tfap2aα* (Mm00495574_m1), *Ngfr* (Mm00446296_m1) and *Sox10* (Mm00569909) (Cat# 4331182, Thermofisher Scientific, Grand Island, NY). The ABI 7300 real-time sequence detection system (Applied Biosystems, Thermofisher Scientific, Grand Island, NY) was used along with the GeneAmp 7900 SDS software (Cat# 4350490, Applied Biosystems, Thermofisher Scientific, Grand Island, NY) to convert data into threshold cycle (ΔΔCt) values.

For genotyping studies, DNA was isolated from mice tail snips collected in sterile 1.5ml microcentrifuge tubes by digestion in 50mM Tris, pH 8.0, 100mM ethylenediaminetetraacetic acid (EDTA) (Cat# 17892, Thermofisher Scientific, Grand Island, NY), 0.5% sodium dodecyl sulfate (SDS) (Cat# L3771, Millipore Sigma, St. Louis, MO) and 20mg/ml proteinase K (Cat# AM2548, Thermofisher Scientific, Grand Island, NY). After overnight incubation, a phenol:chloroform (1:1) phase separation was performed, and DNA precipitated from the aqueous layer using a sodium acetate and ethanol mixture. DNA solubilized in TE buffer (10mM Tris, pH 8.0, 1mM EDTA) was further resolved on 1.2-2.7% agarose gel and probe hybridization performed using the following cDNA primer sequences: *R26R* 5′-AAAGTCGCTCTGAGTTGTTAT-3′ (forward) and 5′-GGAGCGGGAGAAATGGATATG-3′ (reverse); *Mpz* transgene 5′-CCACCACCTCTCCATTGCAC-3′ (forward) and 5′-ATGTTTAGCTGGCCCAA ATG-3′ (reverse); *Tsc2* 5′-CAAACCCACCTCCTCAAGCTTC-3′ (forward) and 5′-AGACTGCCTTGGGAAAA GCG-3′ (reverse) (Integrated DNA Technologies, Research Triangle Park, NC).

QUANTIFICATION AND STATISTICAL ANALYSIS

This investigation was utilized as a pilot study to trace the ontogeny of tumorigenic cells in the $Tsc2^{+/-}$ mice; therefore, the less rigorous resource equation method and upper confidence limit (UCL) approach was

employed to estimate optimal sample size for mouse groups in this pilot study (Festing, 2006). The time required for tumors to develop in *Tsc2*$^{+/-}$ mice was considered, as well as the 80-90% rate of spontaneous tumorigenesis in the kidneys, the number of pups per litter yield (~7 pups), the total number of litters per genotype used, the isogeneity of strains specified for genetic crosses, mouse attrition rate of 8%, and statistical power of 0.8 with double-sided α error of 0.05 (Festing and Altman, 2002; Van Sluyters et al., 2003). Sample sizes in experiments are specified in each figure legend, and all data in the text and figures are expressed as mean $\pm$ SEM. Statistical tests are appropriately justified and performed using a one-way ANOVA with post-hoc Dunnett tests comparing treatment conditions to controls where applicable.